POLITECNICO DI TORINO

Master's Degree in Biomedical Engineering

Master's Degree Thesis

Human glioma infiltration detection algorithm for Optical Coherence Tomography: an AI-Assisted approach based on tissue simulating phantoms

Supervisors	Candidate
Prof. Kristen MEIBURGER	Massimiliano BERTORELLO
Dr. Mengyang LIU	

Academic year 2020/2021

Summary

Gliomas are primary brain tumors with a high rate of malignancy: they account for 28% of all brain tumors and 80% of malignant brain tumors. Maximal tumor resection during surgery is one of the main goals in the treatment of these cancers as it improves the quality of life of the patients and their survival rate. In order to achieve maximal resection, glioma-infiltrated tumor margins must be correctly detected by a system that works in real time. To fulfill this purpose, traditional Magnetic Resonance Imaging (MRI) presents several limits, like elevated costs and a bulky device, and the development of in situ, fast segmentation algorithm is necessary.

The use of Optical Coherence Tomography (OCT) is spreading to a larger range of applications other than ophthalmology and dermatology, due to its non-invasiveness, high resolution, and imaging speed. These characteristics have led this technique to be often associated with segmentation tools in the diagnosis and investigation of several pathologies, even brain cancer.

In this Thesis work, an Artificial Neural Network (ANN) for the detection of human Glioma infiltration in OCT images is presented. The algorithm is trained on acquisitions performed on human tissue-simulating phantoms made of silicone, that can mimic both healthy brain tissue and glioma-infiltrated tissue, and then tested on real tissue acquisitions obtained from brain biopsies. Tissue phantoms are widely used in both clinic and research as they provide a powerful tool for device testing and performances evaluation, without the need of real tissue samples, and they can be easily reproduced. The training and validation phases are carried out on a large dataset of approximately 2 million samples (A-lines) for an extensive amount of time (~500 epochs). Unlabeled OCT images from 4 biopsies of High-grade Gliomas have been used as test set to establish the detection performances: overall results have demonstrated a sensitivity of ~94% and a specificity of ~85%, but higher values can be achieved considering that most of errors come from small defects within the tissue sample that are not present in an intraoperative situation.

This algorithm can be an efficient and useful instrument as OCT-guided surgical tool, providing to the surgeon a 3D representation and classification of the tissue. Further developments will include the reduction of software's computational time, possibly with the use of a dedicated GPU, and a tuning of the algorithm for different wavelengths of the OCT, to create a more general system that can be interfaced to machines with different characteristics.

Acknowledgements

My personal thanks go first of all to my family, for always supporting and sustaining me, even financially, especially in the hardest times.

My relator prof. Kristen Meiburger and co-relator Dr. Mengyang Liu, for granting me this opportunity and giving me all their help and precious advices during the last years.

The Center for Medical Physics and Biomedical Engineering at the Medical University of Vienna, for their welcome and availability. In particular:

Lisa Krainz, for the thousand hours spent assisting me during acquisitions;

David Reichert, my official brain biopsy supplier;

Sam Mathew, for all his hints regarding OCT and phantom materials, as well as the good football chats.

To my adventure mates, Giulia 'I'm-always-late' Rotunno and Simone 'Amarone' Regaldo, who with their personalities have lighted those 5 moths of lockdown.

My close friends, even if they barely know what 'Biomedical engineering', for being always there.

And finally, all the university colleagues that I had the honor to meet during this experience, for all the hours of study, the notes, meals and the curses shared through the years.

Table of Contents

List of Figures

Chapter 1

The Glioma

Gliomas are defined as malignant neoplasms, which are primary brain tumors deriving from glial cells. They constitute approximately the 80% of malignant adult brain tumors but in rare cases they can also affect the spinal cord. Despite their origin is not confirmed with certainty, it is thought to derive from genetic mutations within neuroglial stem or progenitor cells and so, with the hypothesis that specific patterns of genetic alterations shape the clinical features of brain tumors, the use of these patterns for classification and diagnostic purposes rapidly increased in the last years [1]. Gliomas also exhibit characteristics such as uncontrolled cellular proliferation, diffuse infiltration, resistance to apoptosis, and genomic instability. Furthermore, intratumoral heterogeneity and their resistance to chemo- and radiotherapy leads to poor prognosis of glioma patients.

1.1 Classification

For the past century, the classification of brain tumors has been based mainly on the concept that tumors can be classified according to their microscopic similarities with different cells of origin and presumed levels of differentiation. The characterization of such histological similarities has been primarily dependent on light microscopic features in hematoxylin and eosin-stained sections, immunohistochemical expression of lineage-associated proteins and ultrastructural characterization [1]. This approach was therefore based only on microscopy exams and did not take into account the genetic basis of tumorigenesis.

In 2016 the World Health Organization has proposed a new classification of tumors affecting the Central Nervous System (CNS) by introducing molecular parameters related to genetic characteristics. The use of both histology and molecular features has improved the classification, helping to recognize new neoplasm entities, relocate some groups and delete others that do not fit the requirements. Before going in

details about gliomas typologies, it is important to have a general look to the brain tumor category and collocate gliomas in this wide range of pathologies.

The above-mentioned categorization is well represented in Figure 1.1, where a clear distinction between Glioma and non-Glioma is made.

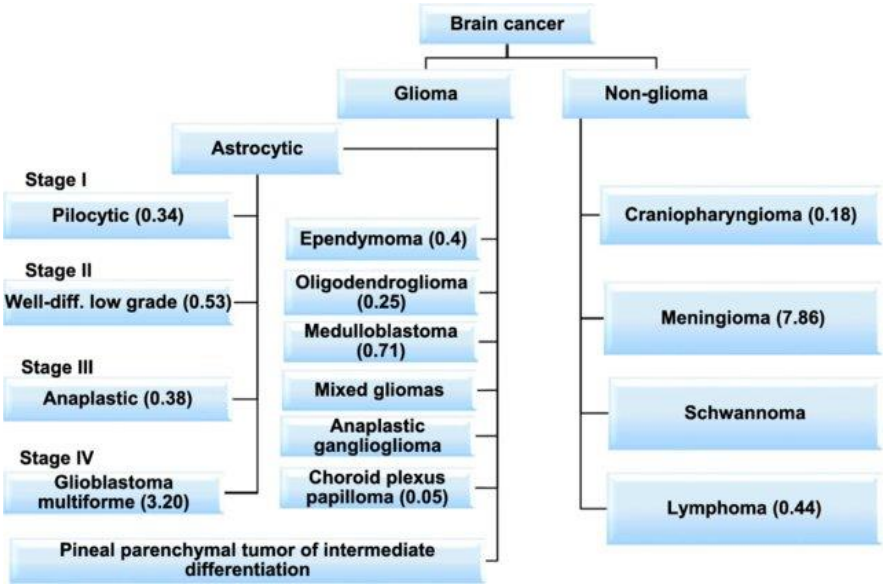

Figure 1.1: Classification of brain tumors as reported from the Central Brain Tumor Registry of the United States (Ostrom et al., 2016). Numbers in parentheses indicates incidence or cases per 100,000 individuals and are age-adjusted to the 2000 United States population *[22]*.

Of course, the branch of interest from Figure 1.1 is the left one. The most common type of glioma is the astrocytoma, which cells show morphological similarities with astrocytes, and this classification principle is adopted for all other types (e.g., oligodendrogliomas with Oligodendrocyte and ependymoma with Ependymal cells). Astrocytoma presents itself four sub-categories basing on WHO malignancy grade, ranging from low malignancy for grade I to high malignant tumor for grade IV. The absence or presence of anaplastic features (such as high mitotic activity, microvascular proliferation, necrosis, etc.) is the criterion adopted to assign the malignancy grade [2]. This evaluation involves not only astrocytomas but all kinds of tumor.

It is important to perform this grading since it can also be used as a marker for one of the main properties of these tumors: **infiltration**. This phenomenon describes the aggressive behavior of glioma cells which exhibit diffuse invasion of the surrounding tissue, complicating the surgical resection and the targeting of the infiltrated area. Whereas other specimens of tumor use the lymphatic and circulatory

system to metastasize into organs, it was shown that the recurrence pattern of gliomas is mainly local and metastases are barely observed.

Further classification can occur considering other aspects, such as:

- **Location** of the cancer: within the brain it can arise in different positions, like in the pons, in the frontal area or the optic nerve, etc.

- **Differentiation patterns** (like pilocytic or myxopapillary).

- **High-grade** and **Low-grade**: classification that consider the severity of the lesion and its extension, other than the infiltration grade. Only 10% are low-grade gliomas and they are mainly labeled as grade I and II; the remaining are considered high-grade gliomas and belong to WHO grade III (anaplastic astrocytoma, anaplastic oligodendroglioma, and anaplastic ependymoma) and grade IV (glioblastoma multiforme). The last one cited, glioblastoma or simply GBM, is the most common and malignant primary brain tumor. 90% of these tumors have demonstrated to relapse in close proximity (1–2 cm) to the primary tumor while only a small portion have been observed to relapse at more distant sites [3].

- **Age** of the patient: generally, gliomas are diagnosed after the 40 years of age. GBM have the tendency to occur even later, but low-grade astrocytomas (like pilocytic astrocytoma) and diffuse midline gliomas have higher incidence on children.

These aspects, however, are not considered by the WHO classification and as already mentioned, only histological and molecular findings are exploited. Table 1.1 summarizes the classification strategies presented in this paragraph.

1.1.1 Genetic features

Within the wide range of genetic parameters that can be useful to classify brain tumors, the two most relevant have been evaluated by WHO: the mutation of the IDH enzyme and 1p/19q co-deletion. The basic classification algorithm is reported in Figure 1.2.

Isocitrate dehydrogenase (IDH, also known as NAD^+) is an oxidoreductase class enzyme that is involved in Krebs' cycle. Its mutation is a key concept to understand molecular pathogenesis of gliomas and is much more common in WHO

grade II and III gliomas (60–80%) than in glioblastomas (5–10%), but in young patients there are more episodes of GBM that exhibit a mutated IDH. Distinction is made between two cases denoted ad IDH mutant (where the molecule has undergone mutation) and IDH wild-type (unmutated). Although IDH-mutant and wild-type gliomas cannot be discriminated under the microscope, they represent very different tumor entities in terms of molecular pathogenesis and potential therapeutic targets and are used for diagnostic purposes. The most common mutation is IDH1, but IDH2 mutation is also considered.

1p/19q co-deletion (deletion of chromosomal arms 1p and 19q) has considerable importance not only because of its association with oligodendroglioma histology and diagnostic value but also because of its clinical use as a predictive biomarker in case of genotoxic therapies. Co-deletion can be demonstrated with fluorescent in situ hybridization (FISH).

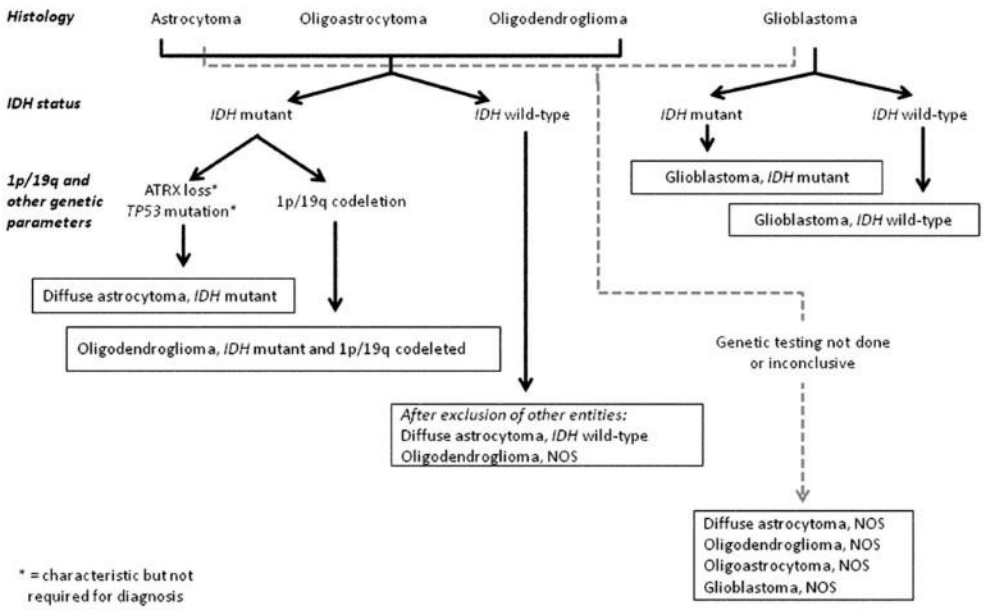

Figure 1.2: Simplified classification algorithm of gliomas. The diagnostic "flow" does not necessarily always proceed from histology first to molecular genetic features next, since molecular signatures can sometimes outweigh histological characteristics in achieving the diagnosis [1].

Other glioma-related molecular factors that can be studied are TERT promoter mutation, TP53 mutation and the loss of nuclear expression of ATRX. The content of this paragraph are summarized in Table 1.1.

Tumour type	WHO grade	Median age at diagnosis* (years)	Survival rate at 2 years* (%; 95% CI)	Survival rate at 10 years* (%; 95% CI)	Common molecular lesions‡	Standard of care§
Pilocytic astrocytoma	I	13	96.6 (95.9–97.2)	91.9 (90.5–93.0)	MAPK activation, most commonly due to *BRAF* fusion or mutation	Observation or carboplatin-based or vincristin-based chemotherapy if resection is not feasible
Diffuse astrocytoma	II	48	61.1 (59.9–62.4)	37.0 (35.4–38.6)	• *IDH1* or *IDH2* mutation • *TP53* mutation • *ATRX* mutation	Observation or radiotherapy or alkylating agent chemotherapy
Oligodendroglioma	II	43	89.6 (88.5–90.7)	62.8 (60.5–65.1)	• *IDH1* or *IDH2* mutation • *TERT* promoter mutation • *CIC* mutation • 1p/19q co-deletion	Observation or radiotherapy or alkylating agent chemotherapy or both
Anaplastic astrocytoma	III	53	43.3 (41.6–45.0)	19.0 (17.3–20.7)	• *IDH1* or *IDH2* mutation • *TP53* mutation • *ATRX* mutation	Radiotherapy or alkylating agent chemotherapy or both
Anaplastic oligodendroglioma	III	49	68.6 (65.9–71.2)	39.3 (35.7–42.8)	• *IDH1* or *IDH2* mutation • *TERT* promoter mutation • *CIC* mutation • 1p/19q co-deletion	Radiotherapy or alkylating agent chemotherapy or both
Glioblastoma	IV	64	14.8 (14.3–15.2)	2.6 (2.3–2.9)	• *EGFR* amplification • +7q/−10q genotype • *PTEN* mutation • *EGFRvIII* expression	Radiotherapy plus concomitant and maintenance temozolomide
Ependymoma	I–III	44	89.7 (88.4–90.9)	79.2 (76.8–81.3)	• *RELA–C11orf95* or *YAP1* fusions (supratentorial) • g-CIMP (posterior fossa) • *NF2* mutation (spinal intramedullary)	Radiotherapy

Table 1.1: Clinical and biological features of gliomas [2].

1.2 Diagnosis

The clinical approach to a suspicious brain tumor is commonly based on the occurrence of neurological deficits over a period of weeks to months or the new manifestation of seizures in a previously healthy individual. These symptoms demand a neurological work-up that includes a neuroimaging assessment. The imaging method of choice to detect a brain tumor is MRI, with and without contrast enhancement, while CT is less frequently used. The diagnostic value of other imaging techniques, such as magnetic resonance spectroscopy or PET, remains to be established. PET in particular, using amino acid tracers, seems to be of value in tumor grading and can aid surgical planning [2].

This first disease screening step is always followed by a histological exam made on tumor resections, preferred to biopsies because it is not limited by small tissue portions and it has a lower risk of grade underestimation. However, as explained in the previous section, these exams are carried out together with molecular markers determination. Molecular features can be investigated on biopsy sample, with the

additional possibility to study silent markers. Biopsies are preferred in patients with extensive or multifocal disease.

1.3 Therapies

The standard approach to treat this class of cancer is a combination of resection surgery with chemo- and radiotherapy. The serious prognosis of glioma demand that patients with are managed in specialized centers according to institutional standard operating procedures and national and international guidelines. Neurosurgeons are in charge of selecting the appropriate procedure and treatment strategy for every single patient, since there is not a generic approach for a determined typology of glioma. Last column of Table 1.1 denotes some of the most diffused care strategies for the listed tumor types.

Chemotherapy is less used than Radiotherapy. This because, during the perioperative period, the patient is undergoing pharmacotherapy and the effect of drug-drug interactions are still unknown for a lot of chemicals. Some drugs can manifest arising of adverse effects like system effects and cognitive impairment. Usually, pharmacotherapy involves the administration of steroids to control tumor associated brain oedema and anticonvulsant drugs if the subject experience seizures during the course of the disease.

1.3.1 Radiotherapy and radiation resistance

Ionizing radiation is one of the gold standards in cancer treatment and it offers a clear survival benefit for most cancer types. Most-established treatment modality for patients with WHO grade II and III gliomas is irradiation of the involved part of the brain, which is commonly applied at 50.4Gy in 1.8Gy fractions for WHO grade II gliomas or 54–60Gy in 1.8–2.0Gy fractions for anaplastic gliomas (WHO grade III). However, it has been demonstrated that the currently applied radiation treatment, using low linear energy transfer (LET) photon irradiation, might favor invasion and migration of gliomas, especially considering glioblastoma multiforme. At today findings are still diverging, since other studies have proven the opposite, but this could be due to differences in the experimental setup such as timing and radiation dose.

Radiation resistance could have two possible reasons: first, the tumor cells only receive sublethal doses; second, the cells utilize their repair mechanisms very efficiently. Glioma cells are supposed to be intrinsically radioresistant and their characteristics of rapid proliferation ad infiltration can enhance this behavior. Figure 1.3 shows the survival fraction of three types of glioma cell lines at different radiation doses, averaged over three considered patients. The response is different for each cell line, in accord with the hypothesis that radiosensitivity is an intrinsic property of the cells.

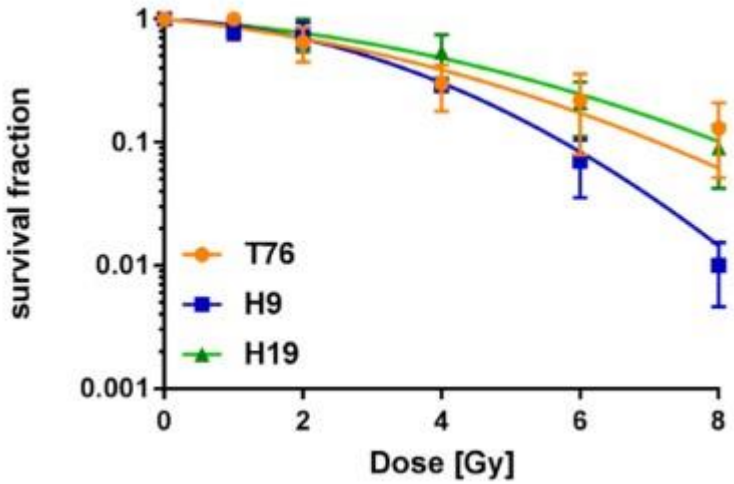

Figure 1.3: Survival fraction of three patient-derived glioma cell lines. T76: glioblastoma stem cell enriched culture; H9: Embryonic stem cells line; H19: Hippocampal fibroblast. Curves are fitted with a linear-quadratic model after low linear energy transfer (LET) irradiation [3].

Two indices that connect radiation dose to the survival rate are considered: D50 and D10 that represent, respectively, the dose at which the 50% and the 10% of cells survive. All three measured cell lines show different D50 and D10 values after low LET irradiation, confirming what previously said (Table 1.2).

Cell line	D50 (Gy)	D10 (Gy)
T76	3.2	7.1
H9	2.9	5.8
H19	3.9	8.0

Table 1.2: D50 and D10 values for the three considered cell lines.

1.3.2 Resection surgery approaches

The goal in brain cancer surgery is to achieve maximal tumor resection. Several imaging techniques are currently being evaluated or already adopted as image-guided surgical tools to assist with brain cancer resection. Magnetic resonance imaging (MRI) provides excellent visualization of soft tissue, but due to its low space resolution it is impossible to detect small defects at tumor margin and intraoperative MRI is cumbersome and expensive. Intraoperative computed tomography (iCT) allows the evaluation for residual cancer but again is limited by a low sensitivity at the tumor periphery. Moreover, these methods are time-consuming, expensive and do not provide continuous real-time intraoperative guidance. Other imaging modalities have been developed lately such as ultrasonography (US), which enables real-time imaging, but has limited contrast and spatial resolution for the detection of brain cancer and can often interrupt the surgery procedure.

A new approach that has become quite popular in recent years is the use of intraoperative fluorescence as wide-field imaging technologies and biomarkers. Within the spectrum of molecular marker adopted nowadays, exogenous fluorescent biomarkers such as 5-aminolevulinic acid (5-ALA) is one of the most successful, especially for its sensitivity towards high-grade gliomas like GBM; however, its performances with low-grade tumors are still limited and controversial [4].

To allow subcellular resolution and label-free imaging capabilities, Raman spectroscopy have been broadly applied for brain tissue biochemical differentiation and glioma infiltration detection, despite its capability of discriminate cancer-infiltrated tissue intraoperatively has not been fully demonstrated yet. Unfortunately, several limitations are associated to this technique, including the intrinsic weakness of the Raman signal, limited imaging depth and field of view (FOV) and slow imaging speed. More recently, coherent Raman Scattering (CRS) and Stimulated Raman Scattering microscopy (SRS) have been explored for brain tumor margin differentiation; however, a definite intraoperative Computer-Aided Diagnosis system for human brain tissue differentiation has not been reported. Therefore, computer-aided diagnosis tools capable of providing continuous, intraoperative and accurate labeling of brain cancer infiltration resection surgery are needed.

1.4 OCT as intraoperative detection tool

To overcome the issues presented at the end of Section 1.3.2, OCT has been evaluated as an image-guided tool for brain tumor resection surgery due to its high resolution and imaging depth (1.5 – 3 mm) similar to the resection depth of cancer infiltrated brain regions [5]. Optical coherence tomography (OCT) is a label-free, non-invasive medical imaging technique capable of continuous, high-resolution, 2D and 3D imaging of biological tissues (see Chapter 2). During an operation, acquisition and data processing speed are of major importance as these kinds of devices work in real time: OCT satisfies the first requirement (fast acquisition, a few seconds maximum) but to accomplish the second goal it must be integrated with a proper classification algorithm able to process and give the results in a brief time interval.

Previous computational methods for OCT-based detection of glioma-infiltrated brain tissue rely on estimating the tissue optical attenuation coefficient from the OCT signal, which performs averaging on multiple A-lines to reduce noise and thus sacrificing spatial resolution. The approach proposed in this thesis work is based on an Artificial Neural Network (ANN) trained on real tissue-mimicking phantoms, capable of making a fast classification of the considered tissue. This AI-aided procedure can distinguish, with high resolution, between healthy tissue and glioma infiltration, giving to the surgeon a helpful tool to maximize tumor resection and hence improving overall survival and quality of life of the patient.

Chapter 2

Optical Coherence Tomography

In the medical environment, *Optical Coherence Tomography* (OCT) belongs to the non-invasive diagnostic class of techniques. It is mainly employed in fields such as ophthalmology and dermatology but in recent times its use expanded to many more. As other optical techniques, OCT arises from the concepts of light diffraction and scattering, events that occur when a wave encounters an obstacle on its path determining a change of its properties (direction, amplitude, wavelength and/or phase).

More in details OCT is based on the principle of **interference**, which describes the phenomenon of two or more waves superposing with each other and generating a new one. The result of this summation is between two limit cases:

- **Constructive** interference: generated by waves in phase.
- **Destructive** interference: generated by waves in counterphase.

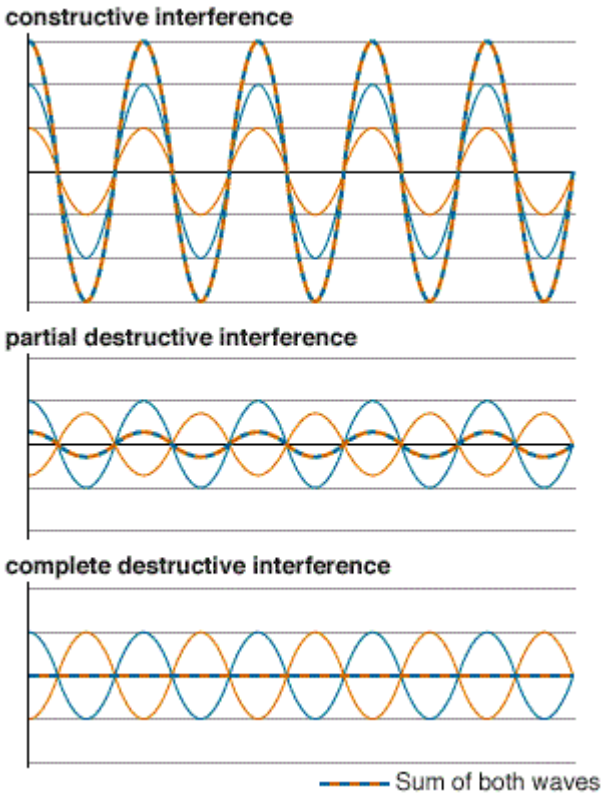

Figure 2.1: Representation of interference between two waves. From the top: constructive, partially destructive and destructive interference.

The working principle of Optical Coherence Tomography exploit interferometry to obtain the reflectivity of the tissue as a function of depth. Since this information is mono-dimensional, the surface under exam is scanned with a raster-scanning technique in order to have 3-dimensional data as output (tomogram). The core of the system is a Michelson interferometer, which performs the measure of light interference [6].

The second key concept is **coherence**. It is related to interference and can be assumed as a measure of similarity between different waves. In fact, two waves are perfectly coherent if their frequency and waveform are identical and their phase difference is constant. This is an ideal assumption, because in a real case two waves remain coherent with each other only for a determined interval of both time and space, respectively defined as '*coherence time*' and '*coherence length*'.

2.1 OCT System

As cited above, the OCT system is based on the Michelson interferometer but the acquisition strongly depends from the light source of the device, which must be a low-coherence source. In the following paragraphs the different parts of a standard OCT set-up will be described.

2.1.1 Michelson interferometer

This basic scheme of this device is reported in Figure 1.1 and, as it is possible to notice, it consists of the following components:

- **Light source**
  (Discussed in paragraph 1.1.2)

- **Beam splitter**
  Optical device that splits the light coming from the source into two separate beams, one transmitted and the other reflected. For this application they are called *reference beam* (light beam that hits the reference mirror) and *sample beam* (light beam that hits the sample). The backscattered lights of the two beams recombine with each other in the beam splitter site and this new beam (*detector beam*) is then directed to the detector.

- **Reference mirror**
  Mirror which reflects the light of the reference beam. It is placed at an opportune distance from the source, and it can be fixed or movable depending on the acquisition technique. All the parts of the system that interact with the reference beam go under the name of '*reference arm*'.

- **Sample**
  Tissue or object that must be imaged. It reflects the incident light of the sample beam depending on its properties, mainly the refractive index.

- **Detector**
  Device that detects the interference information carried by the detector beam. The most employed are photodiodes, which signal is measured as a current because of its better performance in terms of linearity, offset, and bandwidth compared to voltage measurement. The produced photocurrent is proportional to the incident light power and is then converted to voltage.

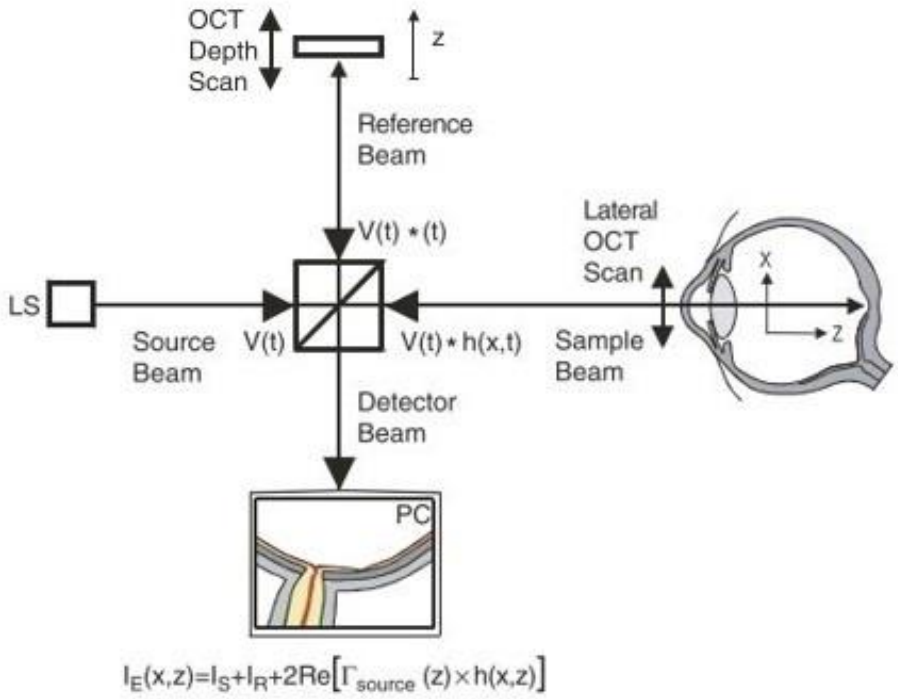

Figure 2.2: OCT scheme based on a Michelson interferometer [6]. V(t) is the analytic signal, h(x,t) is the sample response, $I_E(x, z)$ is the signal intensity at the interferometer exit.

What is measured is the echo time delay of both sample and reference beam, which are then compared to obtain an interference estimation. The sample is scanned in depth (z axis of Figure 1.2) and laterally with different strategies depending on the acquisition technique. As it will be explained in Paragraph 2.2, it is preferable to adopt techniques that do not rely on mechanical movements of parts of the system since it can be a huge source of noise added to the output signal.

2.1.2 Light source

The correct choice of the light source is fundamental to produce a good quality tomogram of the tissue under investigation. Its properties basically rule all the major aspects regarding an OCT acquisition, from the resolution to the penetration depth inside the sample. To be able to obtain a high resolution depth profile, a **low-coherence light source** must be used [7]; this can be easily explained by studying the formula of the coherence length parameter:

$$l_c = \frac{2ln2}{\pi}\frac{\lambda_0^2}{\Delta\lambda} \tag{2.1}$$

In the hypothesis of a Gaussian shape spectrum, λ_0 is the central wavelength and $\Delta\lambda$ is the spectral bandwidth. A perfectly coherent light has $\Delta\lambda \rightarrow 0$ (ideally) which consist in a large value of l_c. Since the coherence length determines the lowest distance at which we can resolve two different points, a wide bandwidth is necessary to obtain a small coherence length and therefore a higher resolution. Equally important is the central wavelength because, for the same bandwidth, the resolution exhibits quadratically decrease with λ_0. The central wavelength is involved not only in depth resolution, but also in lateral resolution and penetration depth, as both parameters increase linearly with λ_0 (see section 2.3). For OCT, commonly used wavelength are located between 600nm and 1600nm.

Particular focus must be putted even to the source power, which is involved in the determination of Sensitivity and Signal-to-Noise Ratio (SNR). High power lead to high SNR and Sensitivity but it can cause damages to the tissue, that's why a compromise must be found between these parameters and tissue tolerance. Generally the most diffused light sources for OCT produce a power of a few tens of mW, but a large spectrum of solutions are present in literature in the 1-400mW range of power.

Last fundamental property for a light source regards the Point Spread Function (PSF) which describes the response of an imaging system to a point source or point object. The source must have a PSF with a narrow half-width and no satellites, which means that the source power spectrum must have a smooth shape.

In Table 2.1 are reported some low-coherence light sources employed in OCT. The most diffused are **Superluminescent Diodes** (SLD), since they span the wavelength range from about 675 to 1600 nm, have output powers up to 50mW and spectral widths up to 70 nm [1], but a lot of alternatives are present from Light Emitting Diodes (LED) to akinetic swept sources.

Light source	$\bar{\lambda}$	$\Delta\lambda$ (nm)	l_C (μm)	Coherent power
SLD	675 nm	10	20	40 mW
	820 nm	20	15	50 mW
	820 nm	50	6	6 mW
	930 nm	70	6	30 mW
	1300 nm	35	21	10 mW
	1550 nm	70	15	5 mW
Kerr lens				
Ti : sapphire laser	0.81 μm	260	1.5	400 mW
Cr : forsterite	1280 nm	120	6	100 mW
LED	1240 nm	40	17	0.1 mW
	1300 nm			
ASE fibre sources	1300 nm	40	19	60 mW
	1550 nm	80	13	40 mW
Superfluorescence				
Yb-doped fibre	1064 nm	30	17	40 mW
Er-doped fibre	1550 nm	80–100	16	100 mW
Tm-doped	1800 nm	80	18	7 mW
Photonic crystal fibre	1.3 μm	370	2.5	6 mW
	725 nm	370	0.75	
Thermal tungsten halogen	880 nm	320	1.1	0.2 μW

Table 2.1: Examples of low-coherence light sources used in OCT [6].

2.2 OCT acquisition techniques

OCT offers a series of possibilities in terms of acquisition, which belong to two major classes: **Time-Domain** (TD-OCT) and **Fourier Domain** (FD-OCT). TD-OCT is the very first technique adopted in OCT while FD-OCT has been developed later to make up for the shortcomings and limits of standard Time-Domain techniques [6]. Before going in details about these two approaches, some mathematical considerations about signal processing and conditioning must be made.

First of all, let's consider the signal at the interferometer exit $\mathbf{I_E}$:

$$I_E(t;\Delta t) \;=\; I_S(t) \;+\; I_R(t) \;+\; G_{SR}(\Delta t) \tag{2.2}$$

As noticeable, I_E is the sum of three different contributes. I_S is the intensity of the sample beam, I_R is the intensity of the reference beam while G_{SR} is the interference term (interferogram), the one of interest. It is equal to twice the real part of the cross-correlation of the analytic signals of sample and reference beam, also called **coherence function**. Since the cross-correlation of analytic functions is also an analytic function, it can be expressed as follows:

$$\Gamma_{SR}(\Delta t) \;=\; \frac{1}{2}G(\Delta t) \;+\; \frac{i}{2}HT\{G(\Delta t)\} \tag{2.3}$$

where Δt is the echo time delay between the two beams and HT{ } means Hilbert transform. What are we interested about is the cross-spectral density function of the beams, which can be obtained by Fourier transforming Γ_{SR}:

$$W_{SR}(\upsilon) \;=\; FT\{\Gamma_{SR}(\Delta t)\} \tag{2.4}$$

where υ represents the optical frequency. By repeating this last operation for all the terms of Eq. 2.2 it is possible to formulate the **spectral interference law**, which is non other that the spectral domain version of Eq. 2.1:

$$S(\upsilon, \Delta t) \;=\; S_s(\upsilon) \;+\; S_R(\upsilon) \;+\; 2Re\{W_{SR}(\upsilon)\}cos(2\pi\upsilon\Delta t) \qquad (2.5)$$

Following this reasoning it is clear that the key term of an OCT signal is the cross-correlation term Γ_{SR}. To extract it from the detector's output $i_G(t)$, which is a photocurrent as already mentioned, the wavefronts of the interfering beams at the interferometer exit are considered to be coplanar with the photodetector's surface; this allows to state that the interferometer's output signal G_{SR} is proportional to $i_G(t)$:

$$i_G(t) \;=\; \frac{q_e\,\eta}{h\,\bar{\upsilon}} \int_{Ar(\boldsymbol{r})} G_{SR}(\boldsymbol{r}, t)\; d^2\boldsymbol{r} \qquad (2.6)$$

$$\downarrow$$

$$G_{SR}(\boldsymbol{r}, t) \;=\; G_{SR}(t) \;\propto\; i_G(t), \qquad (2.7)$$

q_e is the electronic charge, η the quantum efficiency of the detector, h the Planck's constant, $\bar{\upsilon}$ the mean optical frequency, and Ar(**r**) the sensitive detector area. Amplitude and phase of the real envelope of the coherence function can then be calculated, respectively, as:

$$A_\Gamma(t) \;=\; \frac{1}{2}\sqrt{(G_{SR}(t))^2 + (HT\{G_{SR}(t)\})^2} \qquad (2.8)$$

$$\Phi_\Gamma(t) \;=\; arctan\left[\frac{HT\{G_{SR}(t)\}}{G_{SR}(t)}\right] \qquad (2.9)$$

and its final expression is:

$$\Gamma_{SR}(t) \;=\; A_\Gamma(t)\; e^{i\Phi_\Gamma(t)} \qquad (2.10)$$

2.2.1 Time-domain OCT

This technique allows to acquire a tomogram from a sample by performing two mechanical movements: one to obtain the depth profile (z axis of Figure 2.2) and the second to laterally scan the sample. As mentioned, interference is maximum when the pathway of sample and reference backscattered light coincide. To guarantee this, the reference mirror moves along the beam direction in order to change the length of the optical pathway of the reference beam and get the depth information. Lateral scan can be obtained in different ways; the most common method is to employ a rotating mirror that deflects the light hitting the sample.

TD-OCT is the simplest acquisition technique but has different limits. First, mechanical movements of the system's parts can lead to additive noise that corrupts the output signal, mainly due to the presence of actuators and other electronic components. This is why is recommended to perform lateral scanning without moving the sample, because the electric noise carried by the components would be higher than just rotate a small mirror. Second, since Time-domain OCT operates point-like this technique results time consuming because for every point a depth scan is necessary.

2.2.1 Fourier-domain OCT

The main advantage of FD-OCT is that only lateral scan is necessary. Depth-scan information is provided by an inverse Fourier Transform of the spectrum of the backscattered light, so this approach results faster and noise sources are limited. These techniques are based on the treatment of the backscattered field amplitude $A_s(K)$ and differ from each other by the method used to obtain it. As written, A_s is calculated in the K-space, where K is equal to twice the wavenumber k:

$$K = 2k \tag{2.11}$$

In this section, two techniques (the most relevant) are presented: **Spectral-domain OCT** (SD-OCT) and **Swept-source OCT** (SS-OCT).

2.2.1.1 Spectral-domain OCT

For this technique the signal $A_s(K)$ is obtained by using a spectrometer as a detector, consisting of a grating that separates the wavelengths of the hitting light beam and photodetector linear array: signal interference is measured for all the wavelengths present in the collected light (Figure 2.3). Since the interferogram and the cross-spectral intensity $W_{SR}(\upsilon)$ (Eq. 2.4) are FTs of each other , the inverse FT of the spectral interferogram intensity at the spectrometer exit gives the same signal as obtained by low coherence interferometry. SD-OCT is therefore based on the following equation:

$$F_s(z) = FT\{A_s(K)\} \tag{2.12}$$

where $F_s(z)$ is the scattering potential as a function of depth. The spectral intensity at the interferometer exit is:

$$I_{SR}(K) = I_S(K) + I_R(K) + 2\sqrt{I_S(K)\, I_R(K)}\, Re\{\mu(K)e^{i[\Phi_S(K)-\Phi_R(K)]}\} \tag{2.13}$$

$I_S(K)\ and\ I_R(K)$ are, respectively, the power spectrum of sample and reference beam while $\Phi_S(K)\ and\ \Phi_R(K)$ are the spectral phase term of the respective beams. μ(K) is the spectral degree of coherence (=1, if monochromatic light sources are used). The power spectrum of the sample beam is equal to the squared module of the backscattered field amplitude ($I_S(K) = |A_s(K)\}|^2$), which complex amplitude is defined as:

$$A_S(K) = a_S(K)e^{i\Phi_S(K)} \tag{2.14}$$

From these relationships, the Fourier components $A_S(K)$ of the scattering potential $F_s(z)$ cannot be obtained in a straightforward manner. There are two main approaches to overcome this problem:

- **Correlation technique**
  This method implicates to directly Fourier transform the spectral intensity at the interferometer exit, obtaining a function proportional to the autocorrelation function of the total backscattering potential $F(z)$, described as:

$$ACF_F(Z) = ACF_{F_S}(Z) + \sqrt{R} \cdot F_S^*(z_R - Z) + \sqrt{R} \cdot F_S(z_R + Z) + R \cdot \delta(Z) \qquad (2.15)$$

with R = reflectance of the reference mirror, and z_R = reference mirror position. The third term is the one of interest, which is a true representation of the sample's structure (besides a constant factor $\sqrt{R}$). To avoid overlapping of the reconstructed terms, the reference mirror must be put at a position twice the sample depth apart from the next sample interface.

A specific disadvantage of the correlation technique is that the width of the autocorrelation of the object structure in object space equals twice the width of the object structure itself. Therefore, in object space, a range equal to twice the object depth is not available for representing the object structure and a considerable part of the bandwidth of the signal processing system is wasted.

- **Phase-shifting technique**

  Adopted to avoid autocorrelation terms overlapping, it allows to exploit the whole object depth offered by the detector array. Summarily, it consists in the acquisition of two spectral interferograms in phase opposition and then to subtract the second record from the first. The result is an interferogram cleaned from the disturbing autocorrelation terms of the sample. The main drawback is

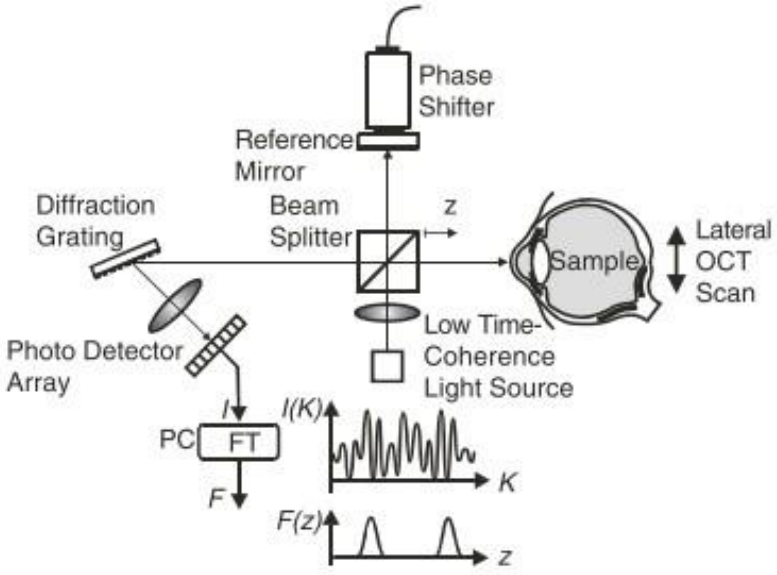

Figure 2.3: Spectral interferometry. FT = signal processor performing the FT. I = spectral intensity; F = scattering potential [6].

that more than one acquisition is necessary, leading to an increase of both working time and collected data.

2.2.1.2 Swept-source OCT

SS-OCT can be interpreted as an evolution of Spectral-domain OCT. With this technique it is possible to gain better resolution in the spectral domain, to have a shorter total acquisition time and to have deeper penetration [8]. The computation is the same as seen for SD-OCT, what changes is the light source and the detector. In fact, this technique's name is given by the introduction of a **frequency swept tunable laser** as source, which sweeps a narrow linewidth laser through a broad optical bandwidth (Figure 2.4). Modern lasers offer a high sweep speed that can reach a few MHz with a wide range of selectable wavelengths; widely accepted values for these quantities are some hundreds of kHz for the swept rate and 20-100nm for the bandwidth.

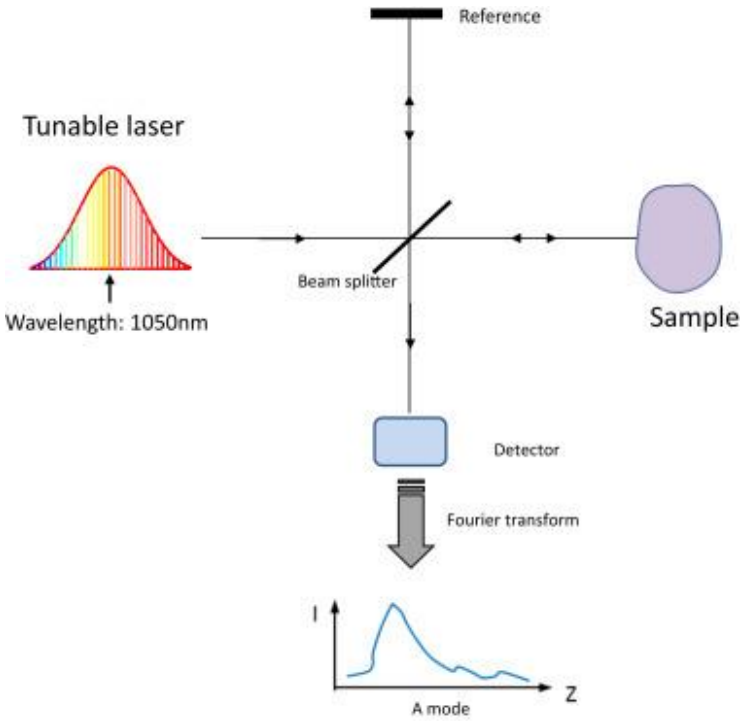

Figure 2.4: Schematic drawing of the swept source optical coherence tomography (SS-OCT) device. The light source is a tunable laser *[23]*.

The other difference is the use of a single photodetector instead of a spectrometer. This also improves speed because the integration at the detector's level is much faster with this device than with an array.

2.3 System properties

In this section, some fundamental properties and parameters of the OCT system will be discussed. Of course, the internal structure and the material of the sample affect the measurement so it's important to take into account all these aspects in evaluating signal quality and its characteristics.

2.3.1 Parameters

Axial resolution

Axial or depth resolution (Δz) of course is one of the most important properties of these kind of systems. It is equal to the coherence length of the light source, proportional to its bandwidth which is the FWHM of the source spectrum. Some considerations about light source properties have already been made in Section 2.1.2 .

$$\Delta z = l_C = \frac{l_{FWHM}}{2} = \frac{2ln2}{\pi}\frac{{\lambda_0}^2}{\Delta\lambda} \tag{2.16}$$

Dispersion too is involved in determining axial resolution; this phenomenon affects the phase of the sample beam wave by introducing a frequency dependence that shifts the signal's phase. It is a property of the tissue which refractive index tends to slow down certain optical frequencies to a greater extent than others. Usually, this phase-shift is corrected via software by using the dispersion compensation technique [9], but it can also be done via hardware (for example, inserting variable-thickness, BK7, and fused silica prisms in the reference arm can balance dispersion).

The dispersion compensation technique applies a phase correction that is computed as:

$$\Phi(\omega) = -a_2(\omega - \omega_0)^2 - a_3(\omega - \omega_0)^3 \tag{2.17}$$

where ω_0 is the mean frequency, a_2 is a coefficient that compensates for the group velocity dispersion imbalance and a_3 compensates for the third-order dispersion imbalance. In most cases, dispersion up to the third order is sufficient assuming that the interferometer arms were approximately dispersion matched initially.

Lateral resolution

Lateral or transversal resolution (Δx) defines the minimum distance at which two points can be distinguished as two separate entities. It is affected by the central wavelength of the source bandwidth and by the numerical aperture (*NA*) of the objective lens, employed to focus the light beam on a point of the sample. Therefore, in order to reach a high value of lateral resolution, it is important to properly design the optic system of the sample arm. Δx is denoted by Abbe's criteria as:

$$\Delta x = 0.61 \frac{\lambda_0}{NA} \tag{2.18}$$

Probing depth

It is defined as the depth at which double scattered photons start to dominate on single backscattered photons and it is related to both sample reflectivity and geometrical characteristics of the sample lens. This phenomenon must be limited since multiple scattered light creates a disturbing background and do not contribute to the object's Fourier spectrum [6]. Of course, it is preferable to have a high probing depth if one is interested to investigate the sample more in deep; this can be obtained by working on the numerical aperture of the sample lens:

$$d = 2n \frac{\lambda_0}{NA^2} \tag{2.19}$$

where *n* is the sample refractive index.

It is necessary to find the proper compromise when considering the NA parameter. In fact, a low value of NA leads to a higher depth of focus but it worsens the lateral resolution and vice versa.

Penetration depth

This parameter is particularly sensible to scattering and absorption properties of the tissue as well as the central wavelength of the light source. Also, in this case a trade-off between penetration depth and axial resolution must be found since higher imaging depths are obtained by using higher wavelengths.

Basing on the acquisition technique, the penetration depth is defined in different ways. In TD-OCT it is given by the reference arm travel range while in FD-OCT it depends on the spectral resolution, defined as $\Delta\lambda_{full}/N$ ($\Delta\lambda_{full}$= total bandwidth of the source; N= number of spectral data points), and it can be calculated using the formula:

$$z_{max} = \frac{{\lambda_0}^2}{4n} \frac{N}{\Delta\lambda_{full}} \tag{2.20}$$

Signal-to-Noise Ratio (SNR)

The SNR of an OCT system, in its extended form, is given by the following equation [2]:

$$SNR = 10\, log\left(\frac{\eta\, P_S}{E_p\, B}\right) \tag{2.21}$$

where P_S is the power at the detector backscattered from a single interface in the sample arm, which is proportional to the A-scan peak height, B is the bandwidth of electronic detection, η is the photodetector efficiency, and $E_p=h\nu_0$ is the energy of the photon associated with the center frequency ν_0. More simply, SNR can be defined as the ratio between mean signal power and noise power therefore it is possible to increase this ratio by increasing the power of the source (directly related to the power of the signal) or by reducing the noise power, which also depends on source power. Noise can have various origins, from detector's electronics (usually specified by the manufacturer) to photocurrent variance.

Sensitivity

Conventionally defined as the inverse minimal sample reflectivity which leads to an SNR equal to 1:

$$S = \frac{1}{R_{S,min}}\Big|_{SNR=1} \tag{2.22}$$

It is directly proportional to the source power and inversely proportional to the electronic bandwidth (B). Usually, with the same bandwidth B and a number of spectral data points equal or greater than 1024, FD OCT systems have 20 to 30 dB of sensitivity advantage over a TD OCT system [8].

2.3.2 Output Data format

As announced before, the final output of an OCT acquisition is a tomogram of the considered portion of tissue, which means that the data is three-dimensional. The punctual depth information is collected over the whole surface of interest by moving the incident beam with a raster-scanning technique (Figure 2.5a).

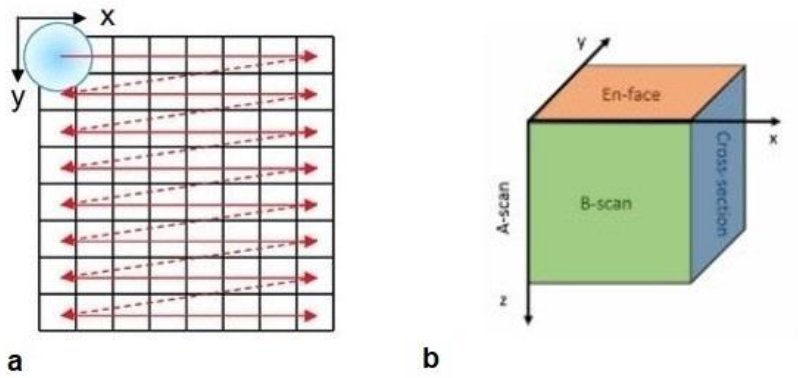

Figure 2.5: a) raster-scanning technique; b) output data format (the cube represents a C-scan).

The acquisition pipeline starts with a single depth scan (**A-scan** or A-line) along the z-direction; after acquiring the first A-line the beam is deflected laterally of a fixed quantity and the operation is repeated until all the depth scans on the x-direction are obtained, which result is an image in the x-z plane called **B-scan**. The beam is moved again on the x-y plane and the entire process continues until the whole volume, named

C-scan, is acquired. The output data, denoted in Figure 2.5b, is therefore a tomogram (C-scan) composed of several images (B-scans) in turn formed by 1-D lines of depth data point (A-scans). The final volume can pe explored in different ways other than looking at a single B-scan or the total tomogram, for example the **En-face** configuration is a representation of all the data point at a certain depth (information on the x-y plane). Another important visualization method is the **Cross-section**, which is an image in the y-z plane and so perpendicular to the direction of a B-scan.

2.4 Characteristics of the employed OCT system

In this section will be given some information about the OCT system of the Center for Medical Physics and Biomedical Engineering at the Medical University of Vienna used to obtain the data for this project.

The acquisition technique is in the SS-OCT category of devices and so, the light source is a swept source laser (SS-OCT-1310, Insight Photonic Solutions, Inc, U.S.) which characteristics are listed in Table 2.2.

Central wavelength	1310 nm
Bandwidth	29 nm
Swept frequency	222.22 kHz
Power	70 mW
Duty cycle	100%

Table 2.2: Swept source laser parameters.

More than 50% of the source power does not reach the sample because most of it is dispersed in the pathway made by the emitted light before hitting the target. Approximately, it can be stated that the remaining power on the tissue is below 20mW. A second consideration is about the duty cycle: since the laser works continuously (DC=100%) there is no rest interval between two consecutive sweeping processes which means that there is no time for the system to switch from a position to the subsequent. To overcome this problem, it has been chosen to skip one sweeping step

after each acquisition and to use that time to pass to the next sample point. Other solutions can be adopted but with this approach no point of the spectrum is wasted.

The interferometer set-up is the same as the one described in Section 2.1.1 with some additions and variations; the system's scheme is represented in Figure 2.6. Light is delivered and carried through the use of optic fibers, which must be periodically checked and cleaned to maintain the system in its optimal conditions. The source beam is directed to a fiber coupler, with a ratio of 75:25, that fulfills the function of the beam splitter. This component separates the light in the two well-known beams: 75% of the power is conveyed to the sample arm while the remaining 25% goes to the reference arm.

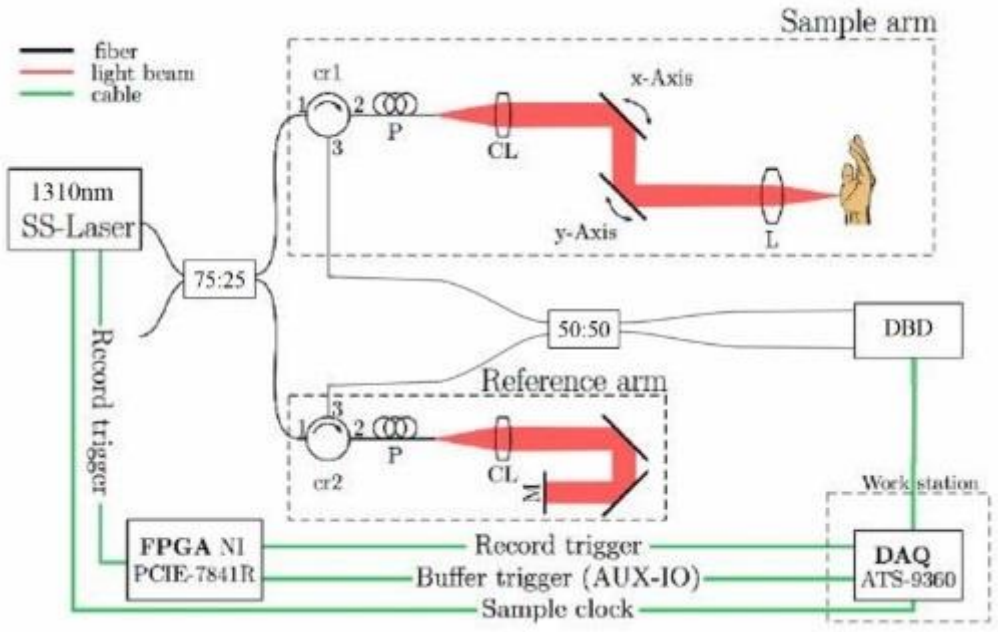

Figure 2.6: OCT system scheme. cr: circulator; P: polarization controllers; CL: collimator; L: objective lens; M: reference mirror; DBD: dual balanced photodetector. The two squares with ratios inside are fiber couplers. Figure adapted from *[25]*.

The reflected beam from the reference mirror makes the same path but in reverse and a second coupler combines it with the beam coming from the sample arm. This signal is then detected by the DBD and passed to the acquisition device (DAQ). In the sample arm, scan on the x-z plane is performed by a galvanometer scanner which is combined to two moving mirrors (one for each axis). It is possible to change the inclination of the sample beam manually by rotating the support on which the objective lens is assembled (Figure 2.8b).

SNR of the system was calculated after acquiring the signal with the sample in position *I* (for this measure, a simple mirror was used as sample) and the background signal *B* (additive noise), obtained by physically blocking the sample beam. Formulation and resulting value are the following:

$$SNR = 10\,log\left[\left(\frac{max(I)}{std(B)}\right)^2\right] = 105.3dB \tag{2.23}$$

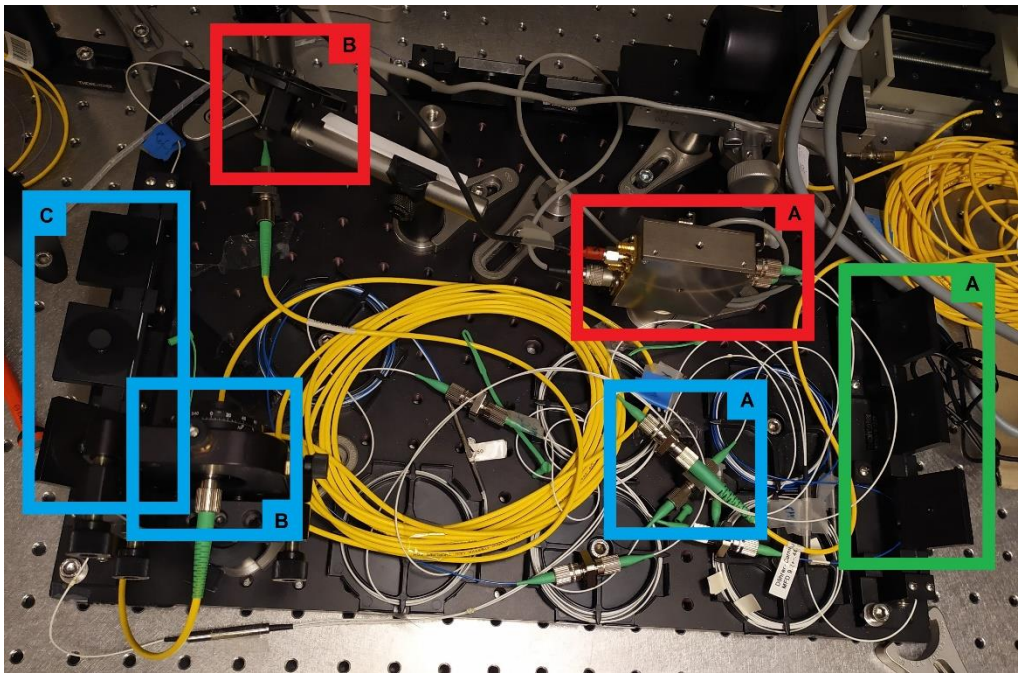

Figure 2.7: board on which are mounted some components of the system. Blue = reference arm (A: fiber coupler; B: collimator; C: polarization controllers). Green = sample arm (not all components are present, A: polarization controllers). Red = general components (A: photodetector; B: power regulator).

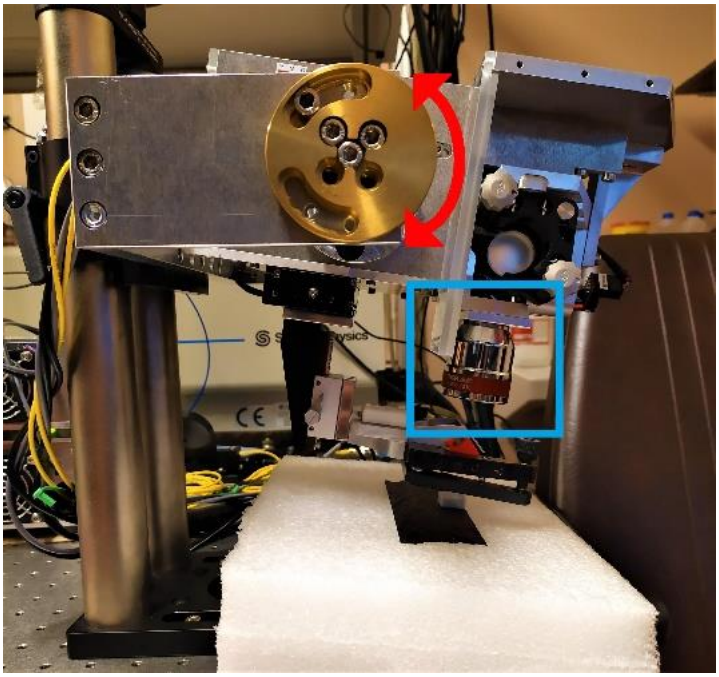

Figure 2.8: Terminal part of the sample arm. Blue = sample lens; Red arrows: system rotation (for beam inclination).

To correctly display the acquired images, axial and lateral image resolution must be calculated. Lateral and axial pixelsize have been calculated in air by using, respectively, a 1mm dot-target (thin glass with highly reflective dots incorporated) and a 1mm thick glass as samples. Obtained values are:

- **Lateral pixelsize** = 19.5µm
- **Axial pixelsize** = 13.7µm

Axial pixelsize has to be divided by the refractive index (RI) of the tissue to get the correct value for the sample under imaging. For example, considering that brain tissue has an RI of 1.40, axial image resolution for this tissue is:

$$Ax_{res} = \frac{13.7\mu m}{1.4} = 9.8\mu m \tag{2.24}$$

Chapter 3

Tissue mimicking phantom development

Tissue-simulating phantoms are of primary importance for the validation of new methods and applications and in both medicine and bioengineering are used for numerous purposes, including: initial system design testing, routine quality control, comparing performances between systems and optimizing specific system properties [10]. To date, several options are available basing on tissue characteristics that we want to simulate such as mechanical, optical and structural properties; in OCT, of course, optical features are the one of interest. Depending on the use, there is another fundamental property to consider, which is **durability**. Lifetime of a phantom relies principally on the selected base material and its origin, which can be natural or synthetic.

Since the focus is on phantom optical properties, the design is not limited by the material physic state (liquid/solid). Liquid phantoms are easier to produce and characterize but suffer of lower durability and high chance of contamination, plus, they must be manipulated very carefully. Solid phantoms suit better for OCT applications because are able to maintain their features for a longer time and offer more possibilities in terms of properties modulation [11]. Before going into details about the materials used to make OCT phantoms, some information about the optical properties of both healthy and cancerous brain tissue will be given.

3.1 Optical characteristics of real tissue

OCT signal is mainly affected by the sample refractive index (for brain tissue n≈1.40) and other two characteristics of the tissue under imaging: **scattering** and **absorption**. They describe the response of the photons when a narrow light beam passes through a medium and loses energy, and they are related with each other by a third property, which is attenuation (μ_t). These data can be obtained from the tissue by determining specific wavelength dependent coefficients:

- **Absorption coefficient** (μ_a): it is a measure of how quickly the beam would lose intensity due to the absorption alone. This phenomenon occurs when photons are not scattered or reflected, and they disperse their energy inside the tissue.

- **Scattering coefficient** (μ_s): this parameter is a measure of the ability of a medium to deflect (scatter) photons out of a beam of light. In OCT only single-scattered photons are considered, while multiple-scattering contributes to the background noise. The sum of scattering and absorption coefficients is equal to the attenuation coefficient μ_t:

$$\mu_t = \mu_a + \mu_s \tag{3.1}$$

- **Anisotropy factor** (g): in optics, anisotropy is a measure of the amount of forward direction retained by an incident photon after a single scattering event. For a material in general, the parameter g is expressed by the mean cosine of the scattering angle of all photons considered, and its value is between 0 and 1. The formula to calculate the anisotropy factor is:

$$g(\lambda) = \int_0^{\pi} p(\vartheta)\, cos(\vartheta)\, 2\pi\, sin(\vartheta)\; d\vartheta = \langle cos(\vartheta) \rangle \tag{3.2}$$

where ϑ is the deflection angle and $p(\vartheta)$ is the scattering pattern, which is measured by a detector that moves circularly around the target while always facing it.

- **Reduced scattering coefficient** (μ_s'): it is a variant of the scattering coefficient which takes into account the anisotropy factor. The purpose of μ_s' is to describe the diffusion of photons in a random walk of step size of $1/\mu_s'$, also defined as scattering length, and it can be obtained in the following way:

$$\mu_s' = \mu_s(1 - g) \tag{3.3}$$

μ_a, μ_s and μ_s' unit of measure is mm^{-1} (or cm^{-1}) while g is a dimensionless coefficient. These parameters are determined from a measurement of the diffuse reflectance and transmittance of light by the tissue sample. To obtain those quantities, the most common procedure consists in an integrating spheres measurement followed by an inverse Monte Carlo (IMC) model to obtain the coefficients from the collected raw data. Figure 3.1 shows the configuration of an integrating spheres system and the flow chart of the IMC analysis.

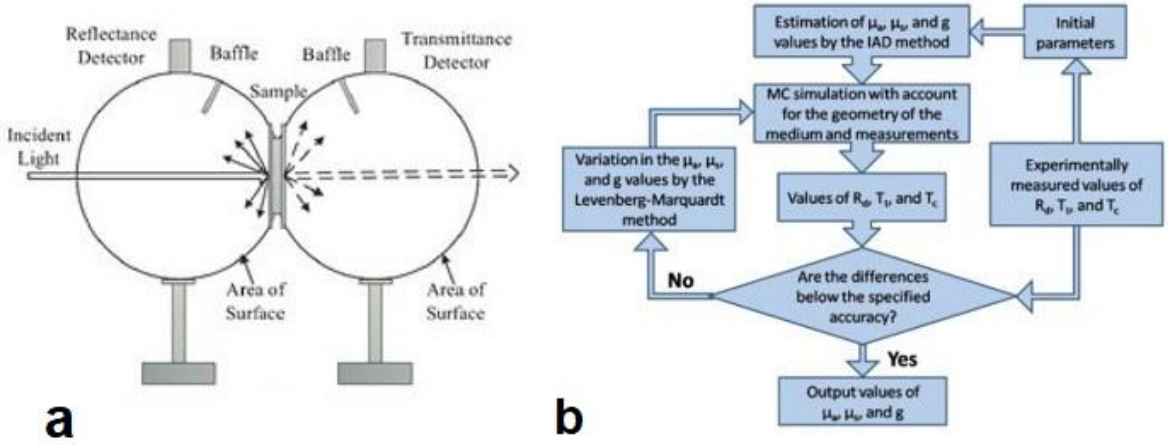

Figure 3.1: a) Integrating spheres measuring system; **b)** example of a basic flowchart of the IMC method (R_d: diffuse reflectance, T_t: total transmittance; T_c: collimated transmittance). Adapted from [13].

Briefly, the device in Figure 3.1a is composed by two spheres with a totally reflecting internal surface, a light source and two detectors (one for diffuse reflectance measuring and a second for diffuse transmittance); baffles are inserted in the spheres to avoid that the light from the source-port directly reaches the detector-port, since this light will have non-uniform distribution. The collected data are than manipulated by using the inverse adding-doubling (IAD) method to obtain more accurate initial approximations of the parameters [12], which will be processed in a iterative way in the IMC model. This procedure continues until the measured and calculated values are matching with a pre-determined accuracy.

Within the numerous articles and experiments that can be found in literature, considering the different approaches used to calculate the parameters and the results obtained, the study reported by *Genina et al*. [13] has been chosen as reference for the values of μ_a, μ_s, μ_s' and g, due to: its recent publication (compared to other similar works), the definition of the coefficients for both healthy tissue and glioma, and the wide range of wavelengths explored (350-1800nm). In fact, most of the papers involve experiments that do not comprehend wavelengths above 1000nm; considering that the

system in use has a central wavelength of 1310nm, using those results could have been an issue. Reported values from [13] are shown in Figure 3.2.

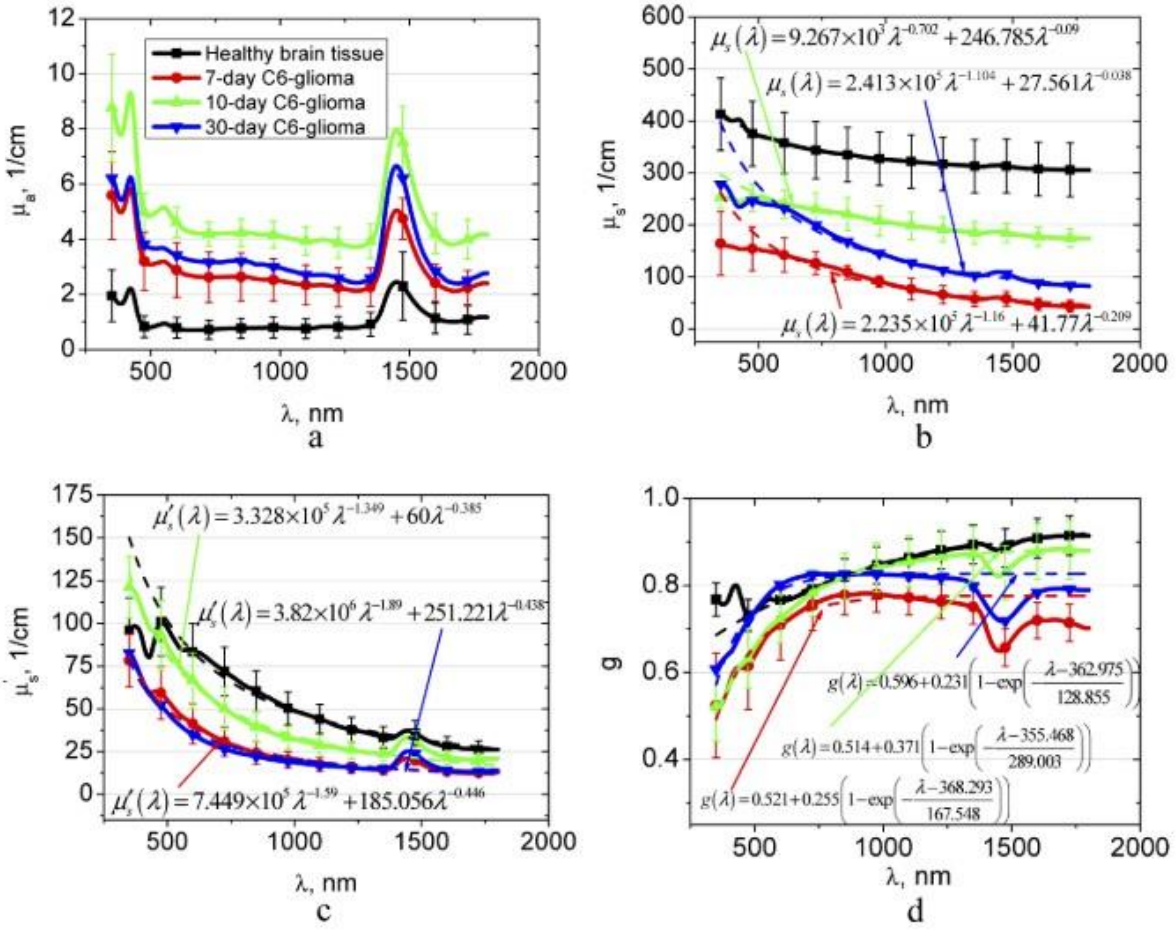

Figure 3.2: Wavelength dependence of the four parameters. **a)** adsorption coefficient; **b)** scattering coefficient; **c)** reduced scattering coefficient; **d)** scattering anisotropy factor. Formulas reported in (b-d) have been used to obtain approximations of experimental data [13].

The experiment consisted in monitoring the variations of the four mentioned parameters after the implant of C6-glioma cells (morphologically similar to human GBM) in healthy rats. Optical properties have been measured before implantation and at different stages of the tumor, for a large spectrum of wavelengths. From the above graphs it can be seen that scattering and adsorption show similar responses in time after tumor implantation, as the first initially decrease, than increase and finally decreases again after 30 days, while adsorption have an opposite behavior. The peaks at ~1450nm correspond to the adsorption band of water. Extrapolated values at ~1310nm are reported in Table 3.1.

Coefficient	HEALTHY (mm^{-1})	TUMOR at 30-days (mm^{-1})
μ_a	0.05	0.29
μ_s	31.55	10.83
μ_s'	3.62	1.24
g	0.885	0.827

Table 3.1: Adopted values of adsorption, scattering, reduced scattering coefficients and anisotropy factor.

3.2 Tested materials

Three types of phantoms with different characteristics have been produced, one in liquid form and two at the solid state.

3.2.1 Intralipid

Intralipid is an emulsion made of Soybean oil and egg Lecithin, diluted in water. It is commonly used for optical measurements due to its constant adsorption properties and easily tunable scattering properties; in fact, the original scattering coefficient of the substance can be reduced by just modifying the dilution rate [14].

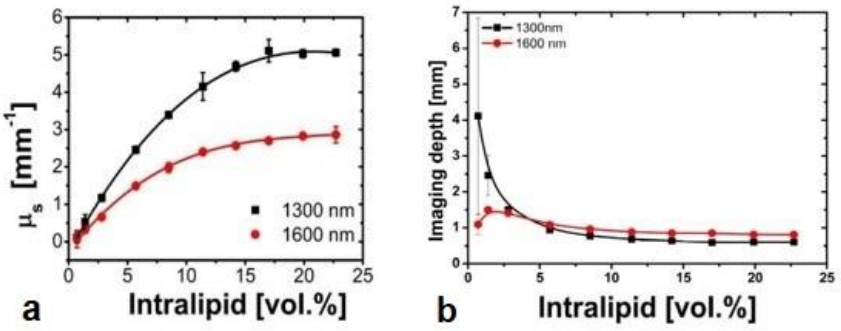

Figure 3.3: Intralipid optical responses at different concentrations for two wavelengths, 1300nm and 1600nm. **a)** scattering coefficient; **b)** imaging depth. The black line is the one of interest. Adapted from *[14]*.

The original solution (produced by Fresenius-Kabi) has a concentration of 20 w./v.% (20g/100mL) but is useful to express it in volume fraction, which is 22.7 vol.%.

Following the results obtained in previous measurements, shown in Figure 3.3, Intralipid has been tested in seven different concentrations (expressed in vol.%): 0.45%, 0.90%, 2.00%, 4.00%, 6.00%, 8.00% and 10.00%. After the preparation, the solutions have been imaged and comparisons with real tissue have been performed (Section 3.3).

Imaging sessions outcomes are reported in Figure 3.4 for the most relevant dilution rates (from 2 to 10%) since concentrations of 0.45% and 0.90% are too far from the real case. The refractive index of the material is considered to be equal to the one of soybean oil, which is n=1.47.

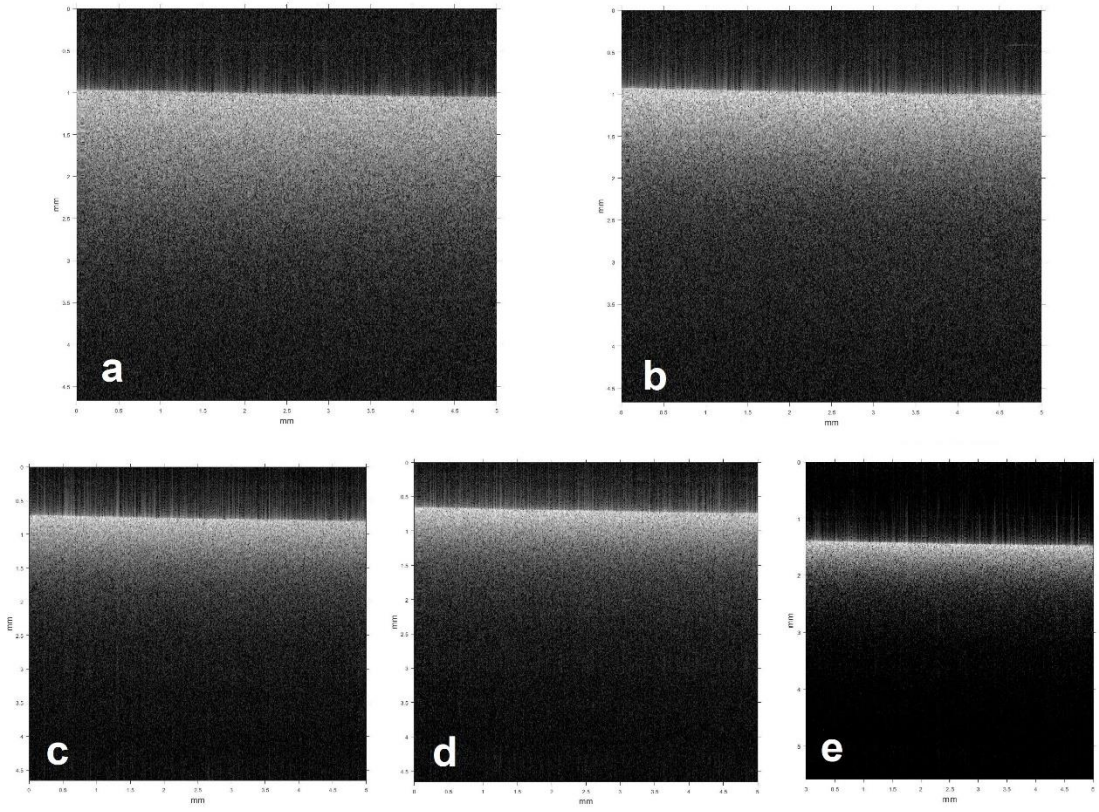

Figure 3.4: OCT images of Intralipid ad five different concentrations (expressed in vol.%). **a)** 2.00%; **b)** 4.00%; **c)** 6.00%; **d)** 8.00%; **d)** 10.00%.

3.2.2 PDMS

Solid phantoms can be subdivided in two main groups, depending on how the scattering properties are obtained: phantoms that rely on additives (micro- and nanoparticles) that induce scattering, and those who possess intrinsic scattering properties [10]. Polydimethylsiloxane (PDMS) is a silicone elastomeric polymer with a refractive index of 1.43, and is included in the first group of materials, since it does not have intrinsic optical properties, as it results transparent during OCT imaging for the considered wavelengths. Many options of additives are available, in this work the choices have been **Titanium dioxide** (TiO_2) **nanoparticles** as scattering medium and **black pigment** as adsorbing agent. The manufacturing process main steps are reported in Figure 3.5 and all the production has been made in the labs of the Center for Medical Physics and Biomedical Engineering of the Medical University of Wien.

Bulk PDMS and curing agent are mixed at a ratio of 10:1, following the instructions provided by the manufacturer, and their quantities are respectively 40mL and 4mL to make a ~44mL phantom. TiO_2 nanoparticles are initially mixed with the curing agent and then the solution is putted in an ultrasound bath for 15 minutes; this is done to limit the presence of Titanium dioxide aggregates in the final product: the curing agent has lower viscosity than PDMS, so it is easier to disrupt those aggregates during a US bath [11]. Bulk PDMS is mixed with black pigment and then mixed again with the curing agent + TiO_2 solution with regular and gentle movements to avoid large air inclusions. The air bubbles that remained trapped into the material are removed by placing the phantom in a vacuum chamber for 15 to 20 minutes. At this point, the product will need to cure for 48 hours at room temperature, but the process can be accelerated by keeping the phantom in an oven (with a temperature of 100°C the phantom can cure in 1 hour).

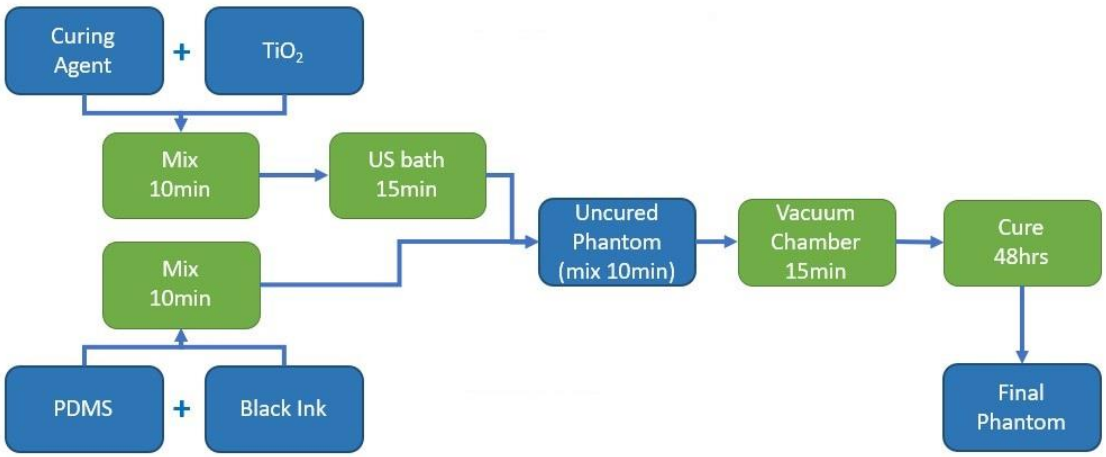

Figure 3.5: PDMS phantom fabrication process. Blue blocks: materials and phantoms; Green blocks: actions/procedures.

To establish the correct quantities of the two additives, a relationship between reduced scattering and adsorption coefficients with the concentrations of TiO_2 and black ink must be found. From similar approaches present in literature ([15], [16]) and, in accord with Mie scattering theory, after producing a series of phantoms with different volumes of additives, two values for each agent have been selected, one for healthy brain tissue mimicking and one for glioma infiltration:

- **Healthy tissue phantom**: 8mg/mL of TiO_2 nanoparticles and 0.2% vol./vol. (40µL) of black pigment.

- **Glioma infiltration phantom**: 4mg/mL of TiO_2 nanoparticles and 0.1% vol./vol. (20µL) of black pigment.

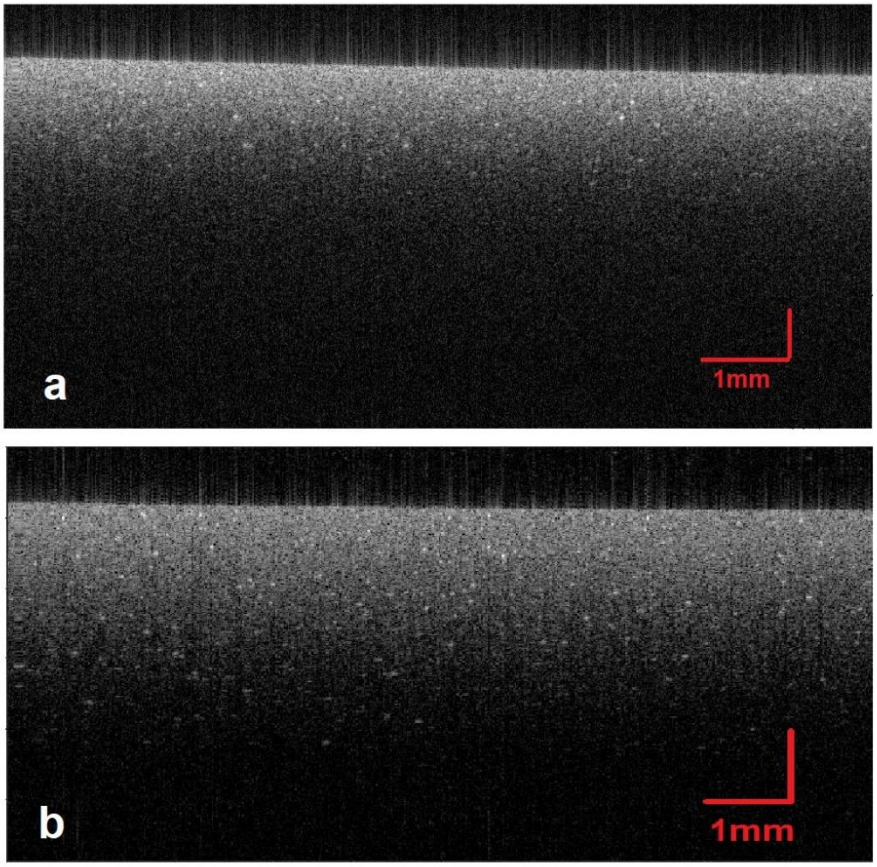

Figure 3.6: OCT images of the two tissue-simulating PDMS phantoms produced. The bright spots are titanium dioxide aggregates. **a)** healthy tissue simulating phantom; **b)** glioma infiltration simulating phantom.

3.2.3 Silicone

These phantoms are made of commercially available silicone rubber (Dragon Skin, n=1.40) which can be easily produced by mixing the two constituent parts (A and B) at a ratio of 1:1. The scattering and adsorbing agents added to the base material, and their respective concentrations, are identical to the ones mentioned for PDMS phantoms (titanium dioxide nanoparticles and black pigment). The fabrication process involves a first step where TiO_2 is mixed with the precursor A (20mL), which is then placed in a US bath for 15-20 minutes, and the black pigment is mixed with the precursor B (20 mL), to obtain a final phantom volume of 40mL. In a second step, the two solutions are mixed together for ~10 minutes and the compound is putted in a vacuum chamber for 10 minutes to extract air inclusions and impurities. The phantom must cure for at least 7 hours but, as well as PDMS, the process can be accelerated by providing heat.

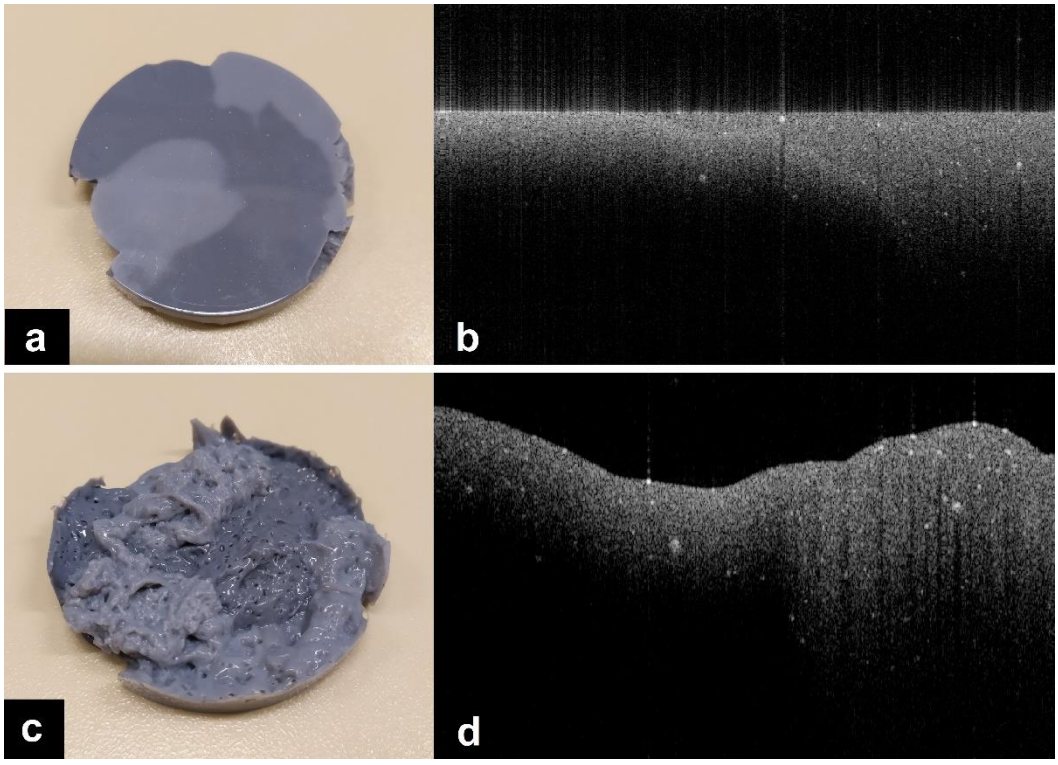

Figure 3.7: Silicone phantom that mimics both healthy (light grey) and infiltrated tissue (dark grey); in this case, the two Silicone phantoms solutions are poured in the same container. **a)** phantom with flat surface and **b)** OCT image of the phantom; **c)** phantom with rough surface and **d)** OCT image of the phantom. In b) and d), the region that exhibits lower penetration depth simulates the healthy tissue, the bright spots are TiO_2 aggregates.

Significant differences with polydimethylsiloxane are the faster curing time of silicone and its higher viscosity at the uncured state. These characteristics make this material suitable for the creation of phantoms with a rough surface (Figure 3.7a) instead of flat; this can be achieved by taking the phantom to a 'partially cured' state (heating at low temperature; e.g., 50°C for 5 minutes), where the material has a high viscosity and can be manipulated without losing its shape.

3.3 Materials comparison

To establish which of the produced phantoms will be used to train the detection algorithm, several criteria have been exploited. In this work, intrinsic characteristics of the materials such as durability, degradation and manufacturing have been considered, as well as an 'envelope analyses' of the A-scans to determine how good the tissue simulating phantom acquisitions can mimic images taken from real tissue.

3.3.1 Intrinsic characteristics

All the three tested materials have optical properties that match, or get close, to the ones of real tissue. Despite the easy production process and its homogenous optical properties, Intralipid has been discarded due to the poor durability (1 to 2 weeks) of such properties in time, while PDMS and Silicone have shown the capability to maintain their optical characteristics for 45 days [16], even 2 months for Silicone. Moreover, manipulating a liquid is more challenging than doing the same with a solid phantom, so silicone derived phantoms are preferred.

Furthermore, as already mentioned, Silicone gives the possibility to create phantoms with a rough surface, useful to simulate a real intraoperative situation since the tissue under investigation will never have a complete flat surface. With Intralipid it is impossible to obtain this feature, and with PDMS is more difficult due to its low viscosity at the uncured state. Another great advantage of Silicone phantoms over other materials is the simple and easily replicable manufacturing process.

3.3.2 A-scan envelope analysis

The comparison between the phantoms A-scan envelopes and real tissue envelopes is the main criterion to determine the quality of the produced phantoms. The envelopes of healthy tissue and glioma infiltrated tissue have been extracted from the imaged biopsies, after [0-1] normalization of the B-scans, and confronted with the values reported in literature [17], confirming those results (Figure 3.8). Normalized envelopes were then obtained from phantom images and the signal has been rescaled between the maximum and minimum of the real tissue signal; this operation is performed to have a standard yardstick for all images, since values from literature and from this Thesis work could have different image processing steps.

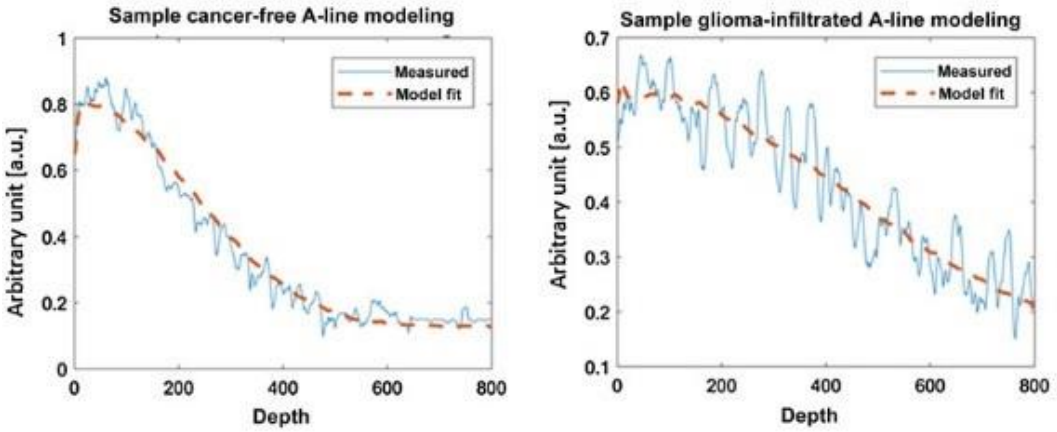

Figure 3.8: Healthy (cancer-free) tissue and glioma-infiltrated tissue envelopes after [0-1] normalization. Adapted from *[17]*.

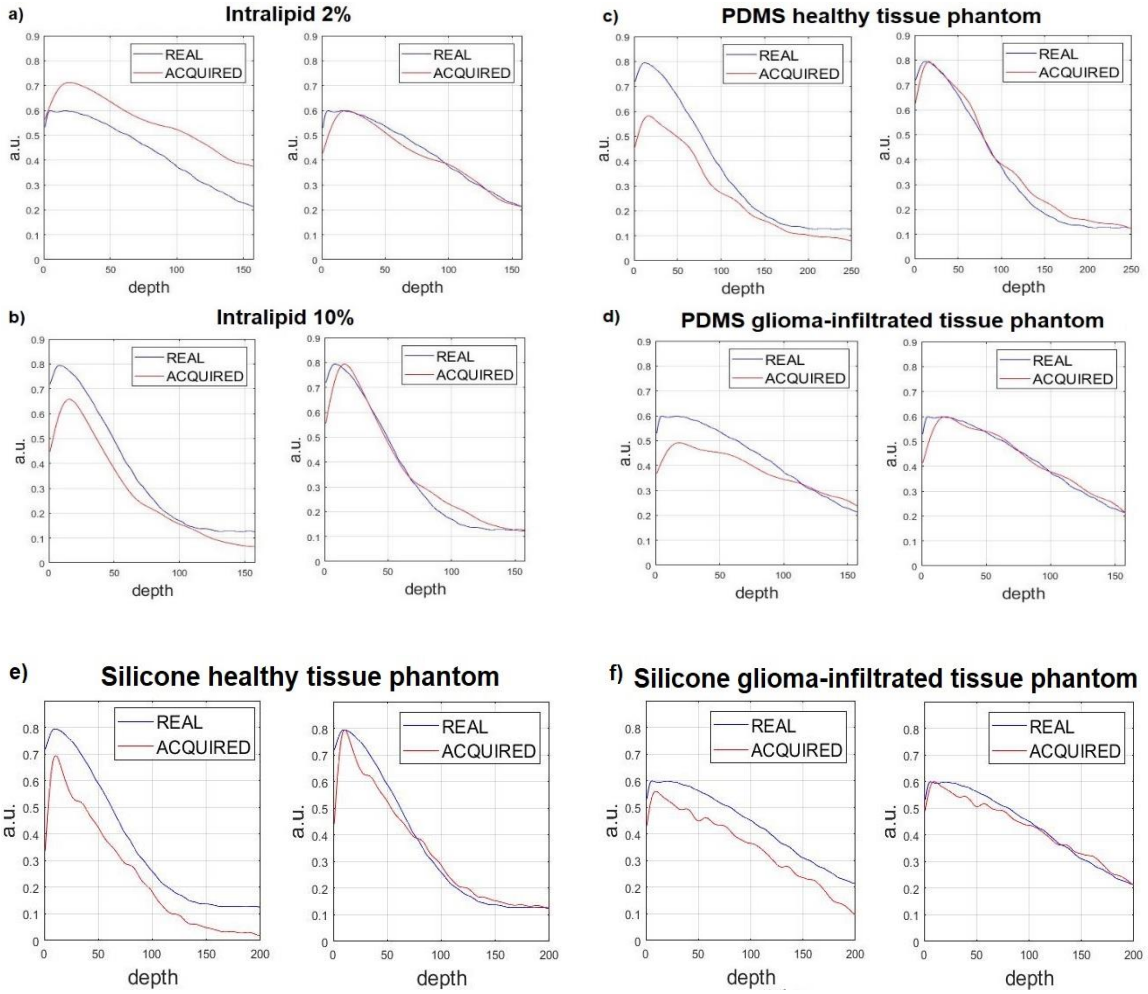

Figure 3.9: Envelope analysis on the tested materials. From **a)** to **f)**, in the left graph the obtained signal is unscaled, while in the right graph values are scaled between maximum and minimum of the real tissue envelope. **a)** Intralipid 2% vol./vol. (at this concentration, Intralipid can simulate glioma-infiltrated tissue); **b)** Intralipid 10% vol./vol. (at this concentration, Intralipid can simulate healthy tissue; **c)** PDMS healthy tissue simulating phantom; **d)** PDMS glioma-infiltrated tissue simulating phantom; **e)** Silicone healthy tissue simulating phantom; **f)** Silicone glioma-infiltrated tissue simulating phantom.

As reported in Figure 3.9, all the selected materials can reach a good similarity with the real case. For Intralipid, the concentrations of interest to mimic the two types of tissue are 2% vol./vol. for glioma-infiltrated tissue and 10% vol./vol. for healthy tissue. For the solid phantoms, this analysis was helpful not only to determine the quality of the work, but also to find the correct concentration of scattering and adsorbing agents. An important detail is the depth range of pixels considered to produce the different graphs, since A-lines are cut at a certain depth before performing the comparison. While Intralipid and Silicone have the same number of pixels for both

healthy and infiltration case, PDMS requires two different cropping height for the two simulated tissues, and this can be problematic since the Neural Network requires the same level of cropping for all the images. For PDMS healthy tissue phantoms the cutting level is too deep (250 pixels considered ≈ 2.4mm in depth), which suggest that additives concentrations could be wrong.

For these reasons, and after the considerations made in the previous paragraph, Silicone phantom acquisitions have been selected to train the Neural Network.

Chapter 4

Data processing and preparation

Raw signals obtained after the acquisition procedure must be correctly manipulated before displaying tomogram images. The general processing steps are independent from the system set-up and the field of view (FOV) adopted during imaging. In this work, a FOV of 10×10mm has been chosen, the length of the A-scans is 2048 points and each B-scan contains 1024 A-lines. The number of B-scans in one tomogram is 1024, so output data dimensions are 1024×1024×2048 (x×y×z). All the processing has been carried out using Matlab R2020b.

Before proceeding with an acquisition session, it is necessary to perform a fast calibration of the swept source laser in which the valid data points are determined. This step is fundamental because the swept wavelengths, during the interferogram recording, present intervals of both valid and invalid data sections. After the calibration procedure, a 'data valid vector' (DVV) text file is generated, containing the indices of the valid points of the interferogram.

4.1 General processing

Each acquisition consists in 16 packages of B-scans (binary files, data format: 16 bits integers), for a total of 64 B-scans per file. Initially, the DVV file is opened (data format: base 10 integers) and the valid data points are loaded, then the program can close the file; once obtained these values the B-scans packages are processed one at time, sequentially, with a little-endian reading bytes order. Data extracted from the package under processing is reshaped into a 2048×65536 matrix, where each column represents an A-scan, which is basically a matrix containing the 64 B-scans concatenated. Only data points written in the DVV must be considered, so the rows that correspond to the values that are not present in that list are canceled. At this point, the data matrix is ready for processing.

Packages are processed in batches of four B-scans at time and every batch undergoes the following steps:

1) **DC removal**: the mean (0Hz component) is subtracted from the signal since it just represents an off-set value added to the signal itself. It can be performed in two ways:
    - Batch mean value calculation and subtraction to all data points.
    - Fourier transform of the batch (performed on the columns), force to zero the first row of the transformed batch (continuous component position) and then inverse Fourier transform the batch to get the initial batch without the 0Hz component; this is the strategy adopted in this work.

2) **Off-set removal**: the A/D waveform digitizer card (AlazarTech) mounted on the used OCT system automatically shifts the data 32752 units up to prevent the presence of negative values inside the dataset; in this way all the data can be represented as unsigned integers. During processing, this off-set is removed from the signal.

3) **Background subtraction**: noisy background must be removed to improve SNR and the quality of the data. This operation can be executed by simply acquiring the background (acquisition with the sample arm blocked) and subtract it from each data point. In alternative, if background is not available, the A-scans of the considered batch are averaged, and the obtained vector is subtracted to all the A-scans of the batch.

4) **Zero padding**: a vector of zeros, long half the number of samples contained in one A-scan, is inserted before and after the A-scan itself, which now has a length that is doubled; this, of course, is done for A-lines contained in the batch. Zero padding is necessary for having a Fourier transform of the signal (step nr. 6) with a high resolution.

5) **Windowing**: a window of samples, with the same length of the A-lines, is multiplied to each A-scan. This step is described in Paragraph 4.1.1, and its effects depend on the type of window.

6) **Fast Fourier Transform**: the batch can finally be Fourier transformed by columns and the spectral copy is then removed; since the Fast Fourier transform produces complex values, the modules are calculated and stored in their respective positions into a pre-allocated matrix with the dimensions of the final tomogram.

When all the batches are processed, the final tomogram is saved. Before performing the above steps, the operator can choose a region of interest (ROI) along the A-scans, to reduce output data dimensions and collect only the considered points.

4.1.1 Windowing of the signal

The correct choice of the window to apply at the signal is fundamental because the properties of the window will determine the characteristics of the output signal, such as resolution and the presence of artifacts. Generally, the windowing procedure introduces the benefit of limiting the presence of surface reflection artifacts, with the drawback of reducing image resolution.

Within the further processing steps (Section 4.2) there is an operation of surface edge detection of the sample: the algorithm that performs this action is strongly affected by reflection artifacts, therefore the application of a window is necessary to enhance its performances. Furthermore, it has been demonstrated that, for this work, despite the window introduces a certain decay of resolution, Neural Network outcomes remain unchanged.

Different types of windows can be applied. The processing code allows the user to select between:

- Hann window
- Hamming window
- Gaussian window
- Chebyshev window
- No window applied

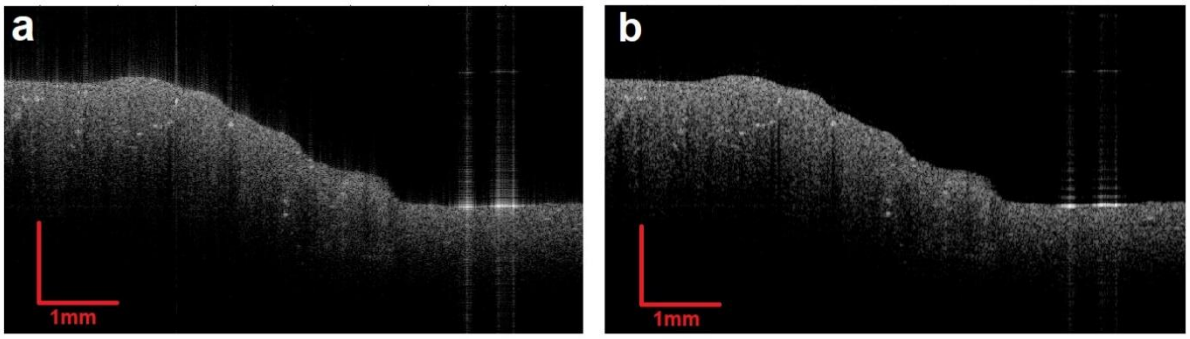

Figure 4.1: Effects of gaussian windowing on an OCT image (B-scan). **a)** B-scan with no window applied; **b)** B-scan with gaussian window applied. Low reflection artifacts are removed, and intense reflections are limited.

After several trials and performances evaluations, the **Gaussian window** was chosen, as it gives the best compromise between reflection artifacts reduction and resolution (Figure 4.1).

4.2 Specific processing

Before entering the Neural Network, data must be prepared with other processing steps that are specific for this purpose. Initially, images are converted in **logarithmic scale** and then **normalized** between 0 and 1. Color properties are then changed to emphasize the tissue in respect to the background, enhance contrast and reduce surface reflection artifacts. To do this, image pixel intensities that are equal or lower than a certain value (0.65 in this Thesis work) are forced to 0, and all the pixels values are than rescaled again between 0 and 1.

At this point, three different operations are performed in sequence: surface edge detection, surface warping and image cropping.

4.2.1 Surface edge detection

Sample surface edge is detected from each B-scan. The process involves first the binarization of the image to create a binary mask containing the tissue pixels, then the upper part of the mask, which carries the edge information, undergoes a few steps of

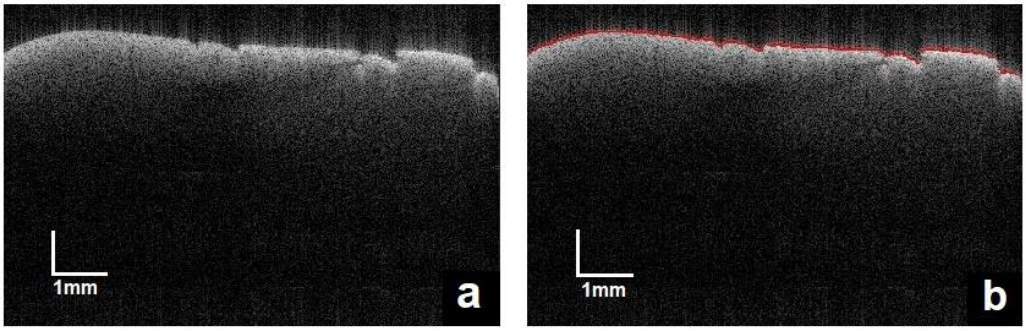

Figure 4.2: Surface edge detection algorithm outcomes. **a)** B-scan of brain tissue before detection; **b)** B-scan after detection algorithm (the red line is the detected edge).

erosion and dilatation. These manipulations have the effect of limiting surface reflection artifacts that generate 'spikes' on the surface (see Paragraph 4.1.1) and optimize surface detection. Sample's upper edge is then extracted from the modified binary mask of the considered B-scan with the **Canny Edge Detection algorithm**, already implemented in Matlab.

Considering that during the general processing a gaussian window has been applied to the data, surface sparks are completely removed by the erosion/dilatation process, exception made for reflection artifacts with particularly high intensity, and the surface edge is detected with great accuracy (Figure 4.2).

4.2.2 Warping

The ANN developed is designed to work only on the tissue, therefore all the parts above the sample must be removed to avoid misclassifications. This can be easily done exploiting the detected edge information, by keeping trace of the edge points coordinates. Each A-scan is shifted up of a value equal to the row index of the corresponding edge point of that A-scan, so the pixels corresponding to the upper edge of the tissue will be positioned on the first row of the image (Figure 4.3).

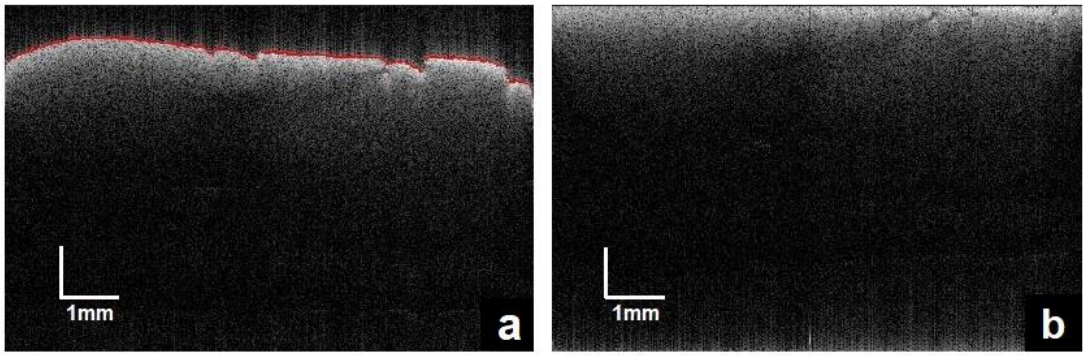

Figure 4.3: Image warping processing step outcome. **a)** Original B-scan with the detected edge (superimposed in red); **b)** B-scan after warping (it is possible to notice that the pixels that where above the edge are translated at the bottom of the image).

4.2.3 Cropping

Final phase of the specific processing is image cropping. As specified in Paragraph 3.3.2, it is fundamental to find the correct depth at which the B-scan must be

cut, since the same value must be applied for both phantom and tissue samples images. After A-scan envelope analysis and considering the Neural Network performances on images with different cutting levels, the determined **cropping depth** is **1.5mm**. Evaluated depth ranges were in the 1-2mm interval, and 1.5mm is the value that guarantees the lowest percentage of misclassifications (Figure 4.4).

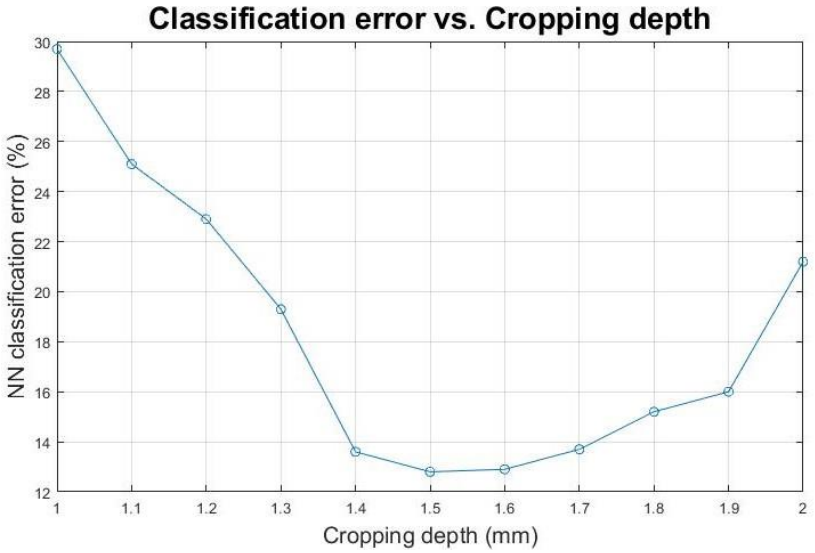

Figure 4.4: Neural Network classification error at different cropping depth values. A depth of 1.5mm (error = 12.798%) is the one that gives the best results in terms of accuracy.

Chapter 5

Artificial Neural Network

Artificial Neural Networks (ANN) are a subset of **machine learning** algorithms that became popular in the early 2000s for their capability of handling large volumes of data. Their structure is inspired by human brain and the core idea is to simulate neurons interconnections and interaction with the use of 'nodes' (artificial neurons) that are grouped in layers. Each node is associated to an activation function, which determines if data can pass to the subsequent layer, and a weight. The algorithm is trained for a certain time, or until the desired accuracy is matched, in which it learns to classify the different input data by updating neuron weights [18]. The approach used in this work is called **supervised learning** since, during the training phase, the network receives both the sample data and its correct classification output (**gold standard**), so that the algorithm can learn by confronting the predicted label with the provided label. Confronts are made by using a **loss-function**, which determines the overall classification error.

The developed Neural Network is a **multi-layer perceptron** network (or deep neural network) that operates in a feedforward manner, with backpropagation from the

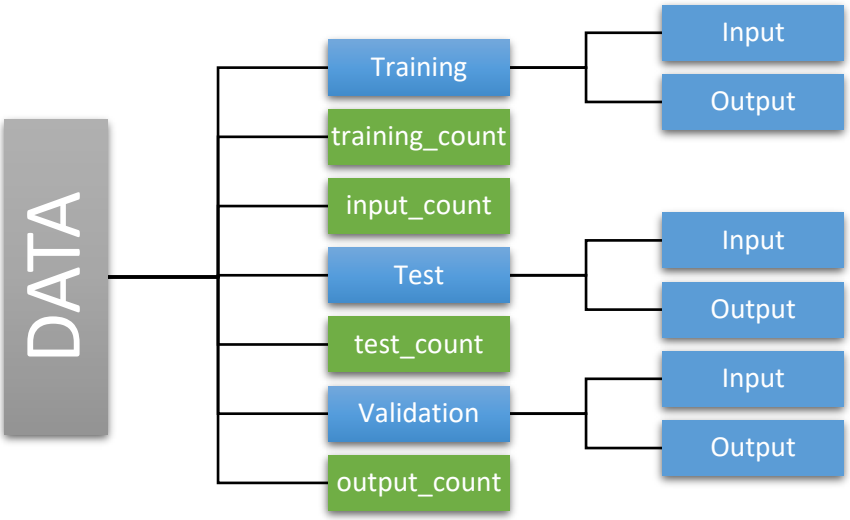

Figure 5.1: Data structure organization. Blue squares: data matrixes or sub-structures; green squares: parameters (integers).

output layer to adjust the weights of the hidden layers. Input data and their parameters are organized in a structure (Figure 5.1) before entering the network, so all the information regarding those data are grouped together.

In details, the data structure includes:

- **Training** sub-structure: here are stored the dataset that will be used to train the network (training set) and its pre-determined output or gold standard.

- **Test** sub-structure: it contains the test data (not the ones used for performances evaluation, but the data to evaluate the training phase) and the relative gold standard.

- **Validation** sub-structure: as well as Training and Test sub-structures, it contains the data matrix for training validation and the respective gold standard.

- **training_count**: number of samples of the training set (in this case, the number of A-scans).

- **input_count**: number of points for each sample (A-scan length in pixels).

- **test_count**: number of samples of the test and validation set (the validation set has the same dimensions of the test set in this work).

- **output_count**: number of output classes, 2 in this case (healthy or glioma-infiltrated tissue).

Since the cropping procedure is based on a value expressed in *mm* (cutting point at 1.5mm), materials with different refractive indexes will have a different final length of the A-scans, in respect to the pixelsize-image resolution conversion. Considering that brain tissue and Silicone refractive indexes are assumed to be equal (n=1.40), the two samples have the same image resolution, and therefore, they will have the same A-scan length after cropping, which is 153 data points.

However, to make the ANN more robust and suitable for various materials, the possibility of having diverse number of pixels after cropping has been taken into account. For all the data entering the network a standard length of 400 points have been chosen, so datasets that have been prepared for neural network processing are all resampled to this value. This means that, for Silicone and brain tissue, 153-points long A-scans are resampled to a 400-points length vector.

5.1 Architecture

General structure

The design of the network presents five layers: an **input layer of 400 points** (A-scan) followed by **three hidden layers** with a decreasing number of neurons, which are 512, 256 and 128 respectively, and an output layer formed by two neurons. Sizes of the hidden layers were determined considering the length of the input layer, and then chose the smallest power of two greater than that value for the first input layer; for the subsequent layers the number of neurons is half the size of the previous layer, exception made for the output layer. This approach has been chosen to optimize computational speed and algorithm performances [5].

To define the final network structure, the performances of different architectures have been tested, with the number of hidden layers ranging from 2 to 4, over a 50-epoch training. Networks with 2 and 3 hidden layers showed similar results in terms of accuracy after the training phase (~94.6%), while performances lower of almost the 10% when networks with 4 hidden layers are considered. A structure with just two hidden layers would be simpler and faster of course, but it could have generalization problems if large datasets, like in this work, are fed to the neural network; for all these reasons, the selected number of layers is three.

Activation functions

Regarding the activation functions, the algorithm gives to the user the possibility of choosing between five options:

- Hyperbolic tangent (tanh)
- Rectified linear unit (ReLU)
- Leaky rectified linear unit (leakyReLU)
- Sigmoid
- Softmax

For this application, the **ReLU** function (Figure 5.2a) has been adopted for the hidden layer neurons, given its non-saturating property and the speed improvement that can give to the training process in respect to other functions, and the **Sigmoid** activation function (Figure 5.2b) was selected for the output neurons, due to the binary nature of the classification [5].

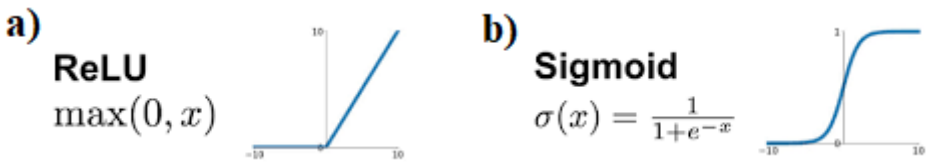

Figure 5.2: Artificial Neural Network selected activation functions expressions and graphic representations. **a)** Rectified linear unit (ReLU); **b)** Sigmoid. Adapted from *[26]*.

Loss-function

Similar considerations can be made about the loss-function, in fact, three pre-implemented functions are present inside the network: Root Mean Squared error (RMSE), Cross-entropy and Binary cross-entropy. RMSE is one of the most common error functions for neural networks, but its non-convex nature can be a problem if the user is interested in inserting an optimization method. **Binary cross-entropy** (Eq. 5.1) was therefore chosen, also because of its faster convergence [19].

$$\mathcal{L}(y, y_p) = y \log(y_p) + (1 - y) \log(1 - y_p) \tag{5.1}$$

In the above expression, y is the true label (taken from the gold standard) and y_p is the predicted label. The loss-function introduces a minimization problem, which means that the optimal set of parameters (wights and biases) can minimize the loss-function value, but since the error is computed for all the samples (A-lines) of a given training set, in this work the attempt is to minimize the average of all computed loss-functions.

Optimizer

Optimizers are algorithms that are allowed to modify some network parameters, such as weights and learning rate, in order to reduce classification errors and improve network convergence. Within the large field of optimizing methods, the most commonly used are Gradient Descent (implemented inside the neural network) and Stochastic Gradient Descent (SGD), which is a variant of the first . Even in this case, the user can select the opportune algorithm:

- No optimizer
- Gradient Descent
- Adaptive Moment estimation (Adam)

- Nestorov accelerated gradient

In the developed ANN, the **Adam optimizer** has been used. It is an extension of the Stochastic gradient descent method, but while SGD keeps the learning rate constant during training, Adam introduces an adaptive learning rate for each network weight exploiting momentums of first and second order (mean and uncentered variance, respectively). In details, the algorithm calculates an exponential moving average of the gradient and the squared gradient, and the decay rates of those averages are controlled by two parameters (Equation 5.2) [20].

$$w_{t+1} = w_t - \frac{\eta}{\sqrt{\bar{\upsilon}_t} + \varepsilon} \bar{m}_t \tag{5.2}$$

$$\bar{m}_t = \frac{m_t}{1 - \beta_1^t} \tag{5.3}$$

$$\bar{\upsilon}_t = \frac{\upsilon_t}{1 - \beta_2^t} \tag{5.4}$$

where w_t is the weight at the *t*-th iteration; $\bar{m}_t$ and $\bar{\upsilon}_t$ are the first and second order momentums; β_1, β_2 and ε are numerical parameters (β_1=0.9, β_2=0.99 and ε=$1 \cdot 10^{-8}$) and η is the learning rate. Despite the computational cost introduced by this method, it provides rapid convergence and it possess the advantage of rectifying vanishing learning rates [21].

Regularization and minimization problem

The introduction of a regularization method is important to avoid overfitting. In a first moment, network performances were evaluated by using the dropout method with different rates, but results showed no significant improvements in classification. The attention moved then towards simpler and well-known strategies like L1 and L2 norms, which introduce a regularization term in the minimization problem. In the resented ANN, a L2 norm was used and so, the error minimization problem equation became:

$$W = arg\min_{W}\left(\lambda\,|w|_2^2 + \frac{1}{N}\sum_{i=1}^{N}\mathcal{L}(y_i, y_{p_i})\right) \tag{5.5}$$

where W are the weights that minimize the argument in round brackets, λ is the regularization coefficient set at 10^{-6}, $|w|_2^2$ is the L2 norm (defined as $|w|_2^2 = \sum_i^n {w_i}^2$) and N the number of samples inside the training set. The function to minimize is composed by two terms: the first is the regularization term introduced by the L2 norm, while the second is the mean value of the loss-functions calculated for all samples.

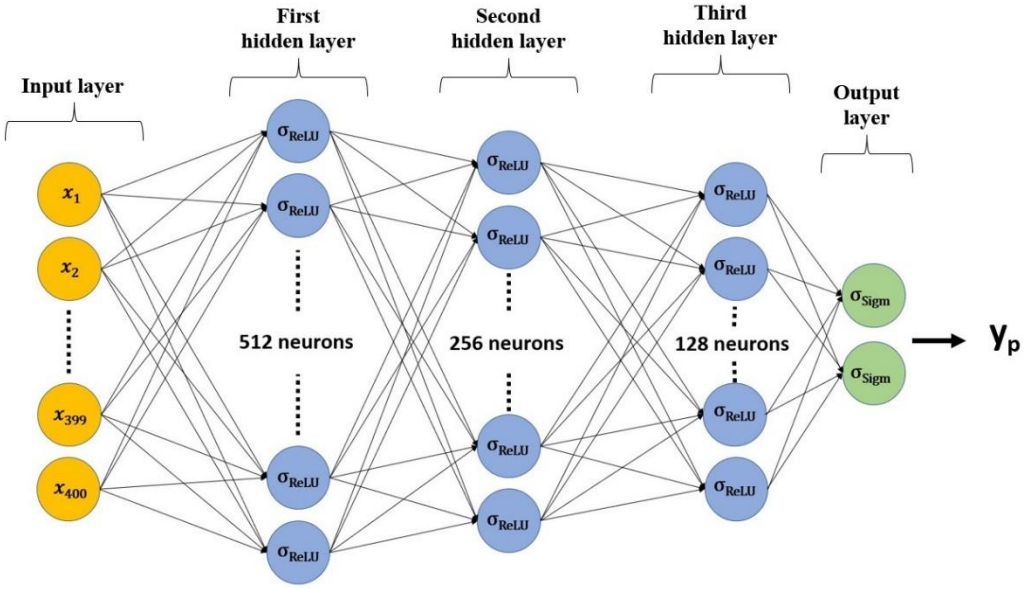

Figure 5.3: Final architecture of the Artificial Neural Network implemented for this study.

5.1.1 Learning rate and batch size tuning

After the definition of the network's architecture, several learning rates and batch sizes were explored, and the respective performances were compared. As a matter of fact, the implemented ANN operates on small batches of samples at the time, not on all the provided dataset, so find the optimal dimensions of that batch is fundamental.

The **learning rate** (LR or η) is a parameter that expresses the speed at which the algorithm can reach the convergence of the learning function, defined as the minimum of the minimization process. As reported in Figure 5.4, the choice of the correct learning rate is crucial since high values allow a fast movement towards the minimum, but they add the risk of never reaching it or, furthermore, inducing a divergent behavior, while small values enlarge too much the training times.

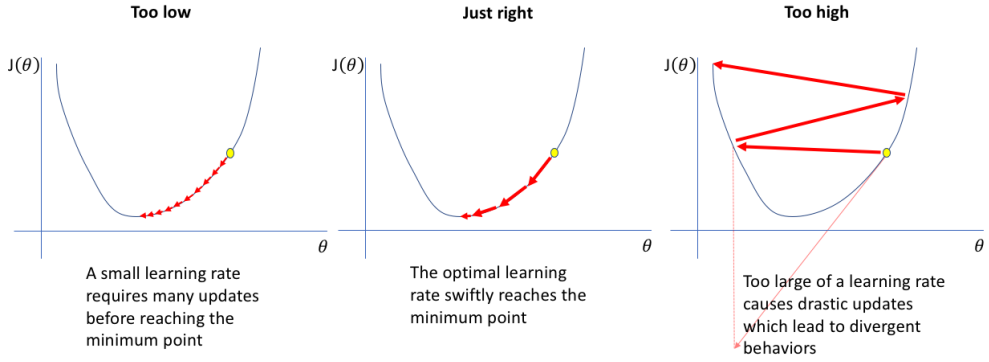

Figure 5.4: Effects of different learning rates on neural network convergence *[24]*.

Together with η, as already mentioned, the tuning procedure is also carried out on the **batch size** (Bs). Evaluated values of these two parameters are:

- $\boldsymbol{\eta}$ = [$1 \cdot 10^{-6}$; $5 \cdot 10^{-6}$; $1 \cdot 10^{-5}$; $5 \cdot 10^{-5}$]
- **Batch size** = [512 ; 1024]

A 60-epoch training is performed, during which all learning rates are tested for each batch size, then the classification results are compared to determine which pair of parameters is the best. First, the comparison was made in terms of labeling accuracy (Figure 5.5a) and the main outcome is that accuracy does not depend from the batch size since there is no significant difference between the reported values, while better classification results were obtained by incresing the learning rate, despite the difference remained low, reaching accuracy values of more than 99%; η values greater than $5 \cdot 10^{-5}$ did not show any improvement and are not displayed in the graphs.

In a second phase, the features used to validate the overall performances, (see paragraph 5.4.1) has been employed to evaluate the tuning of the parameters in a more specific way (Figure 5.5b-c). Interesting results were obtained: the pair of values $\eta=5 \cdot 10^{-5}$ and Bs=1024 is the only one in which specificity and Positive Predicted Value (PPV) are above 99%, while the other couples report lower values. Specificity and PPV

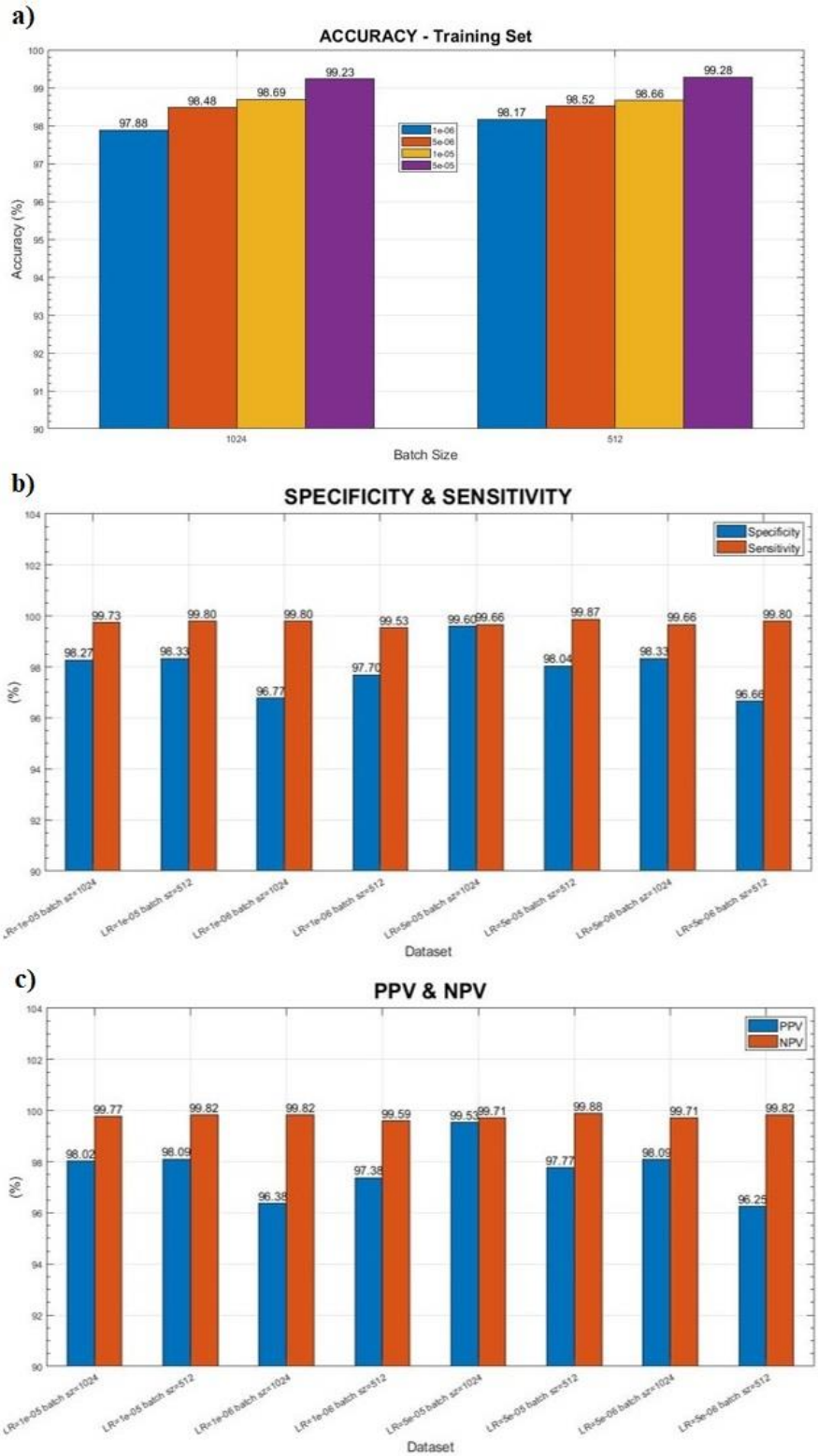

Figure 5.5: Results of the parameters tuning process: **a)** performances comparison in terms of classification accuracy; **b)** comparison in terms of Specificity and Sensitivity; **c)** comparison in terms of Positive Predicted Value (PPV) and Negative Predicted Value (NPV).

are measures of how good the network can recognize the glioma-infiltrated tissue, so it

is extremely important to have the highest value possible of these two features, and that is why the selected learning rate and batch size are: $\boldsymbol{\eta}$**=5·10^{-5}** and **Bs=1024**.

5.2 Training

After the definition of the final structure of the Artificial Neural Network, it is possible to proceed with training the algorithm. During this phase, the data structure presented in the introduction of this chapter is fed to the network, from which it is possible to extract all the information necessary for the task. A-scans are arranged on the rows of the input data, therefore the datasets are transposed before creating the data structure, with final dimensions of $n \times m$ where n is the number of samples in each dataset and m the number of data points for each sample (m=400). The first dimension (n) of test and validation sets is different from the same size of the training set; the choice was to assign to these two datasets a number of samples equal to 1/10 of the corresponding value adopted for the training set.

The dataset from which the three subsets are extracted is composed by the union of **two phantom acquisitions**, which means that the total number of samples (A-lines) is: $Sn = (1024 \times 1024) \cdot 2 = (1048576) \cdot 2 = 2097152$ A-scans. This value is in accord with what reported in similar studies found in literature ([17], [5]) and it guarantees good classification performances with a very low risk of overfitting. Subsets final dimensions are:

- Training set: 1747620×400
- Test set: 174762×400
- Validation set: 174762×400

Training is performed for a total amount of time of **500 epochs** (an epoch is the time required for processing all the datasets one time) with a **target accuracy of 99%**: this high value has been chosen on purpose, considering that the network will never reach this level of accuracy due to the variability between samples and the large amount of samples, so it is sure that the training phase will last until reaching the maximum number of epochs (extensive training). Each batch entering the network is normalized between 0 and 1, and the loss-function is then computed as previously discussed. The algorithm keeps trace of the overall accuracy on training, test and validation sets and displays the results at the end of each epoch. Training results are showed in Figure 5.6 in terms of classification error, with a **final accuracy** after 500 epochs of **98.24%.**

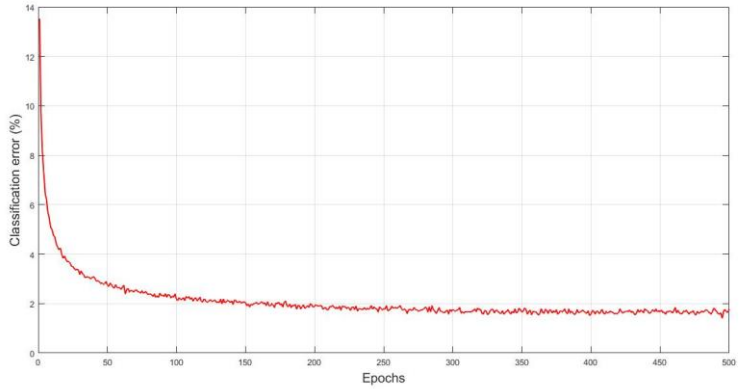

Figure 5.6: Training evaluation over 500 epochs. Final accuracy = 98.24%.

As previously announced, the data on which training is performed is taken from **Silicone** phantom acquisitions. Within several phantoms made for this task, the selected one is a Silicone phantom with rough surface, formed by two regions with different properties, that mimic both healthy brain tissue and glioma-infiltrated tissue. The rough surface is adopted to simulate an intraoperative imaging situation that is as close as possible with the real case and is less subjected to reflection artifacts. The acquisitions of interest are done on two different areas of the same phantom, to assure no variability of the material properties that can merge by using acquisitions taken from different phantoms.

5.2.1 Gold standard creation

Together with the datasets, the neural network must also take as input the respective gold standards. Since it is not possible to directly label each A-scan as healthy or infiltrated, due to the absence of a correct 'map' of the two tissue simulating regions, this information is provided manually from an en-face image of the phantom. The en-face is displayed on the screen and the user can draw, with the cursor, the area corresponding to the infiltration simulating region and create a **binary mask** of that region (Figure 5.7). Eventually, in case the boundary between healthy and infiltration simulating tissue is not clearly distinguishable, it is possible to remove the border region within the materials to reduce the risk of misclassifying those elements and to improve the classification performances; it has been proved that this dimension reduction, if limited to the 15% of the total number of A-scans, does not influence overall accuracy.

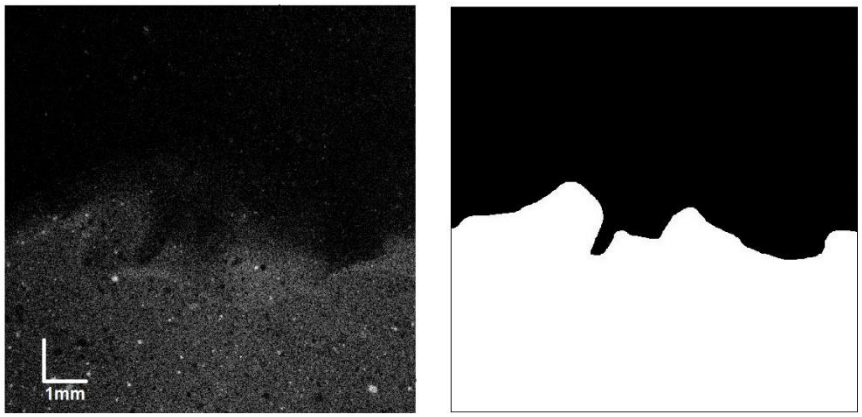

Figure 5.7: Silicone phantom Gold standard creation process. An en-face image (a) at a certain depth (here is set at 2/3 of the total depth) is used to manually create the infiltration region mask (b) that will be used to create the Gold standard.

Samples type of labeling carried out by this network is represented by a binary number:

- **0 1** → Glioma-infiltrated brain tissue
- **1 0** → Healthy brain tissue

The two output neurons return both a numerical value between 0 and 1, then, to obtain the above codification of the solution, the highest of the two outputs is set to 1 and the other is set to 0. Therefore, the designed gold standard is manipulated to obtain a sort of double layer mask, where the first layer represents the labels of the first output neuron (equal to the infiltration binary mask), while the second layer (which is the inverted version of the same mask) represents the labels of the second output neuron. Since the implemented network works by rows, the gold standard matrix is reshaped and transposed just like the previous datasets.

Initially, a threshold was applied to the neuron output values to get the 01-10 codification, but in rare cases (below the 2% of the global classification) outputs equal to 00 or 11 were observed, so this method was discarded in favor of the **majority criterion** explained above.

5.3 Test phase

5.3.1 Brain biopsies characterization

Fresh samples of brain tumor tissue were collected from 10 patients that underwent brain biopsy at the department of neurosurgery of the University Hospital of Vienna (AKH Wien). The samples were maintained immersed in a saline solution, inside an environment with controlled temperature, and taken out from the liquid only during acquisition sessions. Imaging has been performed in two modalities: one in which the tissue is placed on a transparent glass slide with the light hitting the bare surface of the sample (Figure 5.8a), and a second where the tissue was kept in a small 3D-printed box (inner volume: $1mm^3$) containing the same saline solution in which the biopsy is stored or deionized water (Figure 5.8b). The latter method allows the sample to have a more natural shape during imaging, as it is semi-suspended inside the liquid, but it has the drawback of introducing several artifacts like:

- Saline solution surface artifacts and reflections
- Solution induced artifacts (it is possible to observe the merging of high intensity dots or areas generated by particles floating inside the liquid)
- High reflection artifacts when the upper surface of the liquid is in contact with the sample

These artifacts can be limited by using a gaussian window during post-processing, but in general better performances are obtained when the sample is simply putted on a glass as it makes easier the surface edge detection.

The **histopathological analysis** results were obtained after all tissue samples were acquired and are presented in Table 5.1. From a first look, it is clear that not all biopsies are of our interest because only a few are labeled as gliomas (High Grade Glioma in this case) with infiltration characteristics. The useful acquisitions are therefore three,

Patient	Age	Gender	Location	Group	Type
1	78	w	intra-axial, right frontal	B-Cell Lymphom	INF
2	46	w	left, front paramedian	HGG	INF
3	65	m	central right	HGG	INF
4	35	w	intra-axial, frontal		
5	54	w	intra-axial, right frontal	MET	INF
6	68	w	cerebellar, left	MNG	TUM
7	52	m	extra-axial, medial sphenoid bone	MNG	TUM
8	66	m	extra-axial, temporal	MNG	TUM
9	70	m	intra-axial HSG, right	MNG	TUM
10	74	w	left, temporal	HGG	INF

Table 5.1: Histopathology analysis results for the 10 biopsies. HGG: High Grade Glioma; MET: Metastasis; MNG: Meningioma; TUM: Tumor core tissue; INF: infiltrative tissue.

which are the ones classified as HGG and INF (infiltration tissue), and they correspond to biopsies taken from patients 2, 3 and 10. In details:

- **Patient 2**: Glioblastoma multiforme of grade IV (GBM IV); diffuse and recurrent infiltration of the Central Nervous System, IDH-mutant.
- **Patient 3**: Glioblastoma multiforme of grade IV (GBM IV); infiltration with moderate cell density, IDH wild-type.
- **Patient 10**: Glioblastoma multiforme of grade IV (GBM IV); moderately dense glial tumor tissue, moderately dense infiltration, IDH wild-type.

Since the above analysis does not provide a punctual information about the sample, as it is entirely labeled as INF or TUM, in accord with the Department of Neuroscience that performed the exam it has been made the hypothesis that **no healthy tissue is present** within the samples. This is a major drawback because the absence of one of the two tissues investigated in this work does not allow to assess the algorithm performances with the adopted metrics. However, after a careful examination that comprehended A-scan envelope analysis, and a visual evaluation of the samples, it has been demonstrated the presence of a small piece of healthy brain tissue inside the biopsy taken from patient number 10. With this new hypothesis it is possible to calculate the validation features.

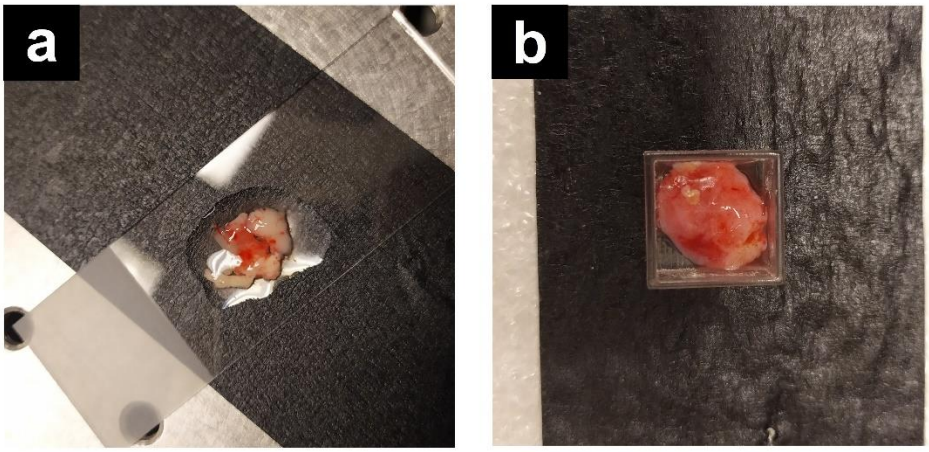

Figure 5.8: Brain tumor bipsies imaging modalities. **a)** Sample on a glass; **b)** sample inside a small 3D printed box filled with saline solution or deionized water (box made of VeroClear).

5.3.2 Validation features

Four metrics have been chosen for validation purposes and all of them can be obtained from a **confusion matrix** computed during the performance evaluation phase. The confusion matrix is a 2×2 table that collects the classification results for the two types of tissue under investigation, by keeping trace of the correct predictions and the misclassifications. From Figure 5.9, it is possible to notice that the term 'Positive' is associated to the presence of glioma-infiltrated tissue, while the term 'Negative' is referred to its absence, so the presence of healthy brain tissue.

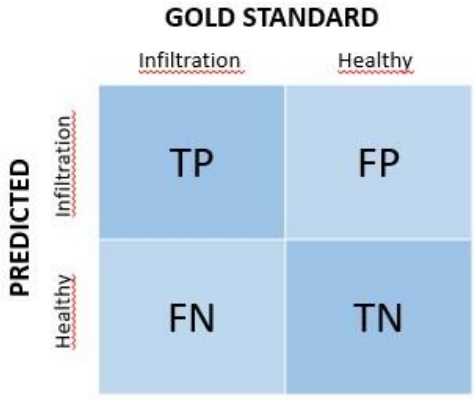

Figure 5.9: Confusion matrix created during the performance evaluation phase.

The selected features can quantify the detection accuracy of the algorithm by comparing the predicted class with the gold standard. All four metrics are expressed by dimensionless numbers in the 0-1 range, which are then converted to percentage values. The features are:

- **Sensitivity**

It measures the capability of the network to identify the true positives, which in this case means how well it can detect the infiltration. Sensitivity can be calculated from the ratio between the number of true positives (infiltrated tissue labeled as infiltration) and the number of samples that are actually glioma-infiltrated:

$$Sensitivity = \frac{TP}{TP + FN} \tag{5.6}$$

- **Specificity**

It defines how well the network can detect the true negatives, represented here by healthy tissue samples. Its computation is the ratio between true negatives (healthy tissue labeled as healthy) and the samples that are actually healthy brain tissue:

$$Specificity = \frac{TN}{TN + FP} \tag{5.7}$$

- **Positive Predictive Value** (**PPV** or Precision)

PPV expresses the probability that a sample labeled as glioma-infiltrated tissue is truly and infiltration sample. It can be calculated by the ratio between true positives and the number of samples labeled as infiltrated tissue:

$$PPV = \frac{TP}{TP + FP} \tag{5.8}$$

- **Negative Predictive Value** (**NPV**)

NPV follows the same concept of PPV but for healthy tissue. It represents a measure of how precise the network is in detecting healthy tissue A-scans, equal to the probability that a given A-line classified as healthy is actually a healthy tissue A-line:

$$NPV = \frac{TN}{TN + FN} \tag{5.9}$$

5.3.3 Performance evaluation

When everything is set, brain sample images can be fed to the network. It can happen that some acquisitions include in their respective tomograms some parts of volume which are not part of the sample, this because the field of view of the system is larger than the biopsy dimensions. In that case, it is necessary to delete from the dataset those A-scans that do not carry any information about the tissue, and this is done by looking at the surface en-face image of the already processed acquisition and, eventually, cut out from the image those border sections where the sample is not present (Figure 5.10).

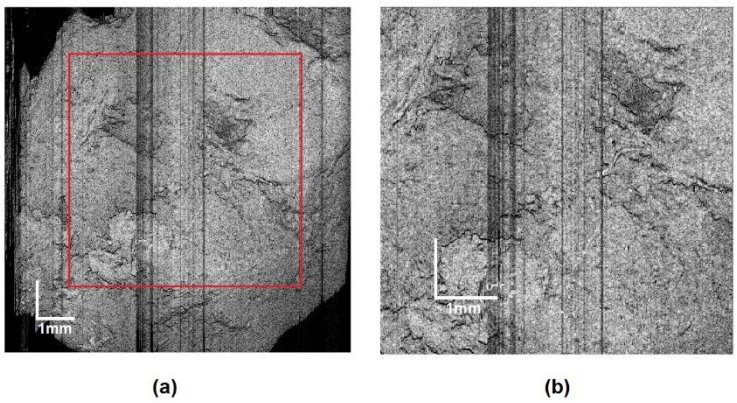

Figure 5.10: Sample volume cropping. **a)** Original en-face at 0-depth of the sample with the cropping area in red; **b)** cropped volume.

To evaluate the performances, the algorithm must know the correct labeling of the tissue, and so the gold standard: it can be obtained with the same method adopted for the creation of the phantom gold standard (Paragraph 5.2.1), taking into account that

the designed masks will not be perfectly matching the two regions because, even if limited, there is always a small difference between the contours of the drawn region and the actual tissue area. Considered this aspect, the network performs the classification and the predictions are confronted with the gold standard, resulting in the generation of the confusion matrix. Once the classification is over, the validation features are computed from the values reported in the matrix, along with the **total error** parameter which expresses the number of misclassifications, and results are displayed on the screen (Eq. 5.10).

$$Error = 1 - Accuracy = 1 - \frac{TP + TN}{TP + FP + FN + TN} \tag{5.10}$$

Together with these metrics, the algorithm displays at video two images in the same figure box: the first is an en-face image (at 0mm depth, which can be assumed as a picture of the sample surface) of the input volume, while the second is the same image to which the classification results are superimposed with a color codification.

The final output is a 3D plot of the sample surface that shows the neural network outcomes on the input volume. Surface information are taken from the surface edge detection procedure performed during the specific processing of the data, which have been saved, and are combined with the color-coded map of Figure 5.11a to generate the three-dimensional rendering of the results.

5.4 Optimization

Overall network performances can be enhanced by a further processing of the computed output. This optimization step arises from two statements:

1. It is unlikely to find small regions of infiltration, as well as healthy tissue, surrounded by A-scans labeled as the opposite class. For example, a few neighboring A-scans classified as infiltration tissue positioned in the middle of an area completely labeled as healthy brain tissue, will be treated like misclassifications and so, the predicted class of those samples will be changed; this reasoning is valid also in the opposite case.

2. Misclassifications mostly occur for A-lines belonging to the B-scans that show severe surface reflection artifacts, where the high-intensity reflections have the power to attenuate the other pixels of the image.

Following these hypothesis, two types of corrections have to be carried out to improve network performances. To satisfy the first statement, the optimization algorithm works the color-coded map of the results, from which are extracted two binary masks, one for each class of tissue. For both masks, the algorithm searches for **areas under 0.05mm^2** (approximately 208 pixels) and, in the results map, converts the label of those pixels to the opposite one. As will be presented in Chapter 6, this step improves the quality of the classification by reducing the errors of almost 3%.

Fulfilling the second assertion is more complicated, since it is due to a phenomenon that is unpredictable for location and intensity and does not depend on the characteristics of the algorithm. High intensity surface reflections have a consistent impact over the other parts of the B-scan already in the acquisition phase: the pixels where the reflection occurs have a value, after normalization, that is equal or close to 1, while the rest of pixel intensities are heavily downscaled, resulting in a B-scan of low quality and deprived of its depth information content (Figure 5.11). This is a well-known problem in OCT and it is easily solvable by just adjusting the angulation of the light beam on the sample. Unfortunately, the irregular surface of the sample makes it very difficult to find the perfect beam direction that suppresses these artifacts, since it

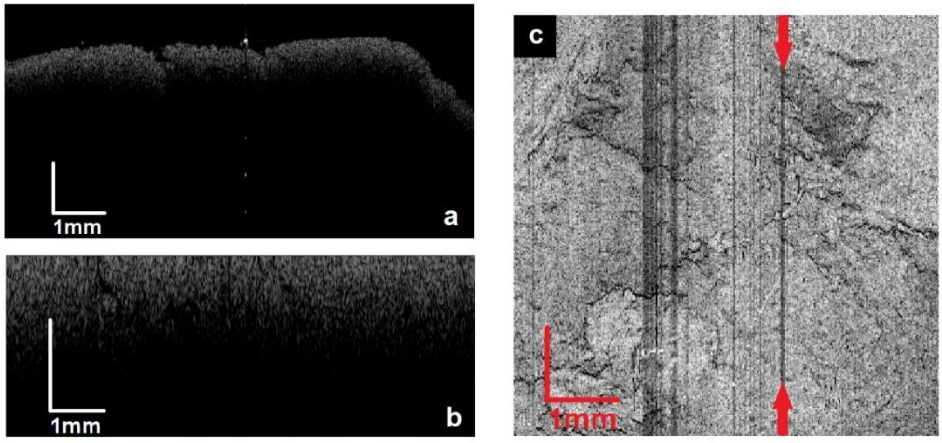

Figure 5.11: High intensity reflection artifacts corruption in Patient 10 acquisition. **a)** B-scan showing a point with high intensity, with other pikels downscaled; **b)** same B-scan after all processing steps; **c)** en-face of the tested volume (red arrows indicate the B-scan presented in (a-b)).

is likely probable that there is at least one point of the surface that shows perfect reflection (the light hits the sample perpendicularly).

Considering the possible intraoperative application of this algorithm, the surgeon can prevent this occurrence by rotating the probe beam or changing its position: the network will recompute the classification and those errors will be eliminated. Otherwise, if the problem is limited to a few B-scans, a correction via software can be applied by replacing those images with an average of the adjacent B-scans. This type of approach is not valid for a large amount of consecutive corrupted B-scans, since the area of real tissue substituted with interpolated images could hide and infiltrative/healthy region that would be lost with the averaging procedure, therefore it has been implemented only for maximum 5 consecutive B-scans.

Chapter 6

Results

6.1 En-face map of results

When the network has finished processing the volume, the algorithm first displays on the screen four images: the en-face image at zero-level (0mm depth) of the input data, the gold standard, a color-coded map with the classification results and the same map after optimization. The codification is simple:

- **Green**: healthy brain tissue
- **Red**: glioma-infiltrated brain tissue

Figures 6.1, 6.2 and 6.3 show the results for the three biopsies selected for the performances evaluation phase, which belong, respectively, to patients 2, 3 and 10.

The dimensions of these images, expressed in mm, refer to the effective measures of the test volumes after cropping the borders of the tissue samples. For each sample, the total area of 10×10mm has been reduced using the following values:

- **Patient 2**:
  x-direction range (columns) = 2,842mm – 8,644mm
  y-direction range (rows) = 1,166mm – 9,653mm

- **Patient 3**:
  x-direction range (columns) = 2,845mm – 9,927mm
  y-direction range (rows) = 1,040mm – 7,593mm

- **Patient 10**:
  x-direction range (columns) = 2,000mm – 8,000mm
  y-direction range (rows) = 2,000mm – 8,000mm

As expected, the misclassified areas that are still present after the optimization procedure, belong to parts of the samples that have inner defects (like holes) or show the corruption of pixel intensities due to several reasons, for example, reflection artifacts.

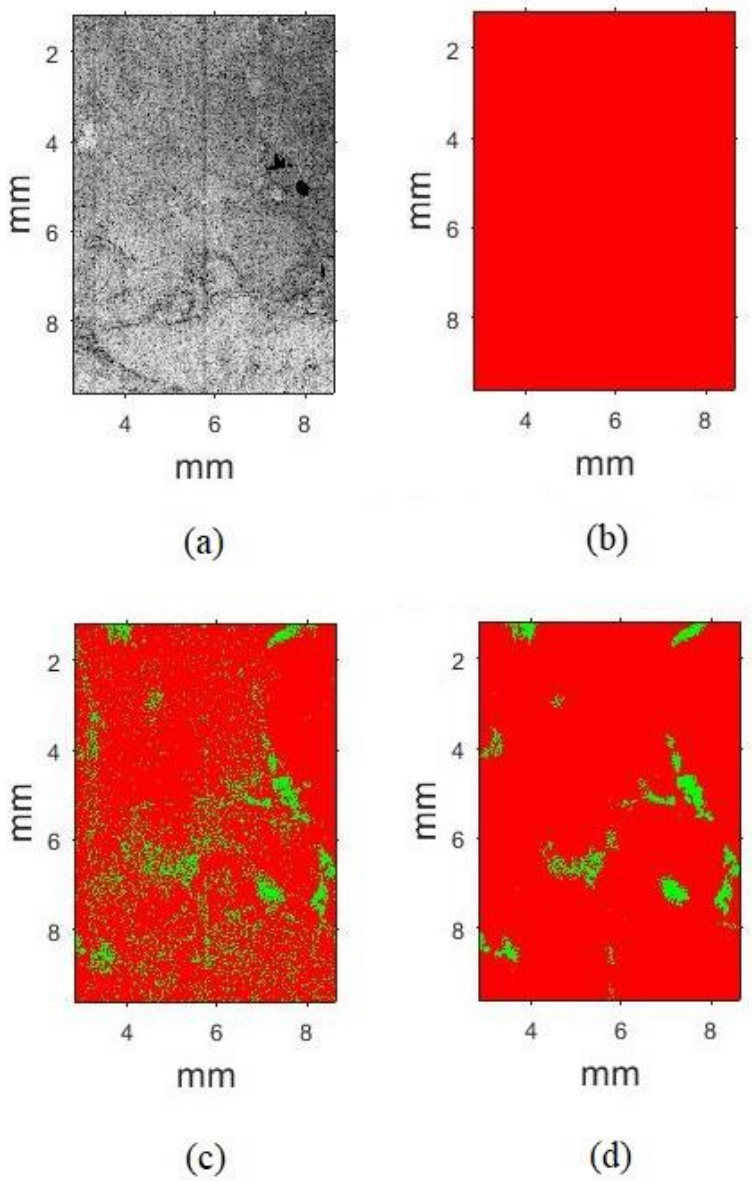

Figure 6.1: Final results of the classification algorithm for the sample of Patient 2 (red = infiltration, green = healthy tissue). For this patient, the sample includes only glioma-infiltrated tissue. **a)** En-face image a 0-depth of the test volume; **b)** Gold standard of the test volume (the sample of patient 2 includes only glioma-infiltrated tissue); **c)** color-coded map of the results before optimization; **d)** map of the results after optimization.

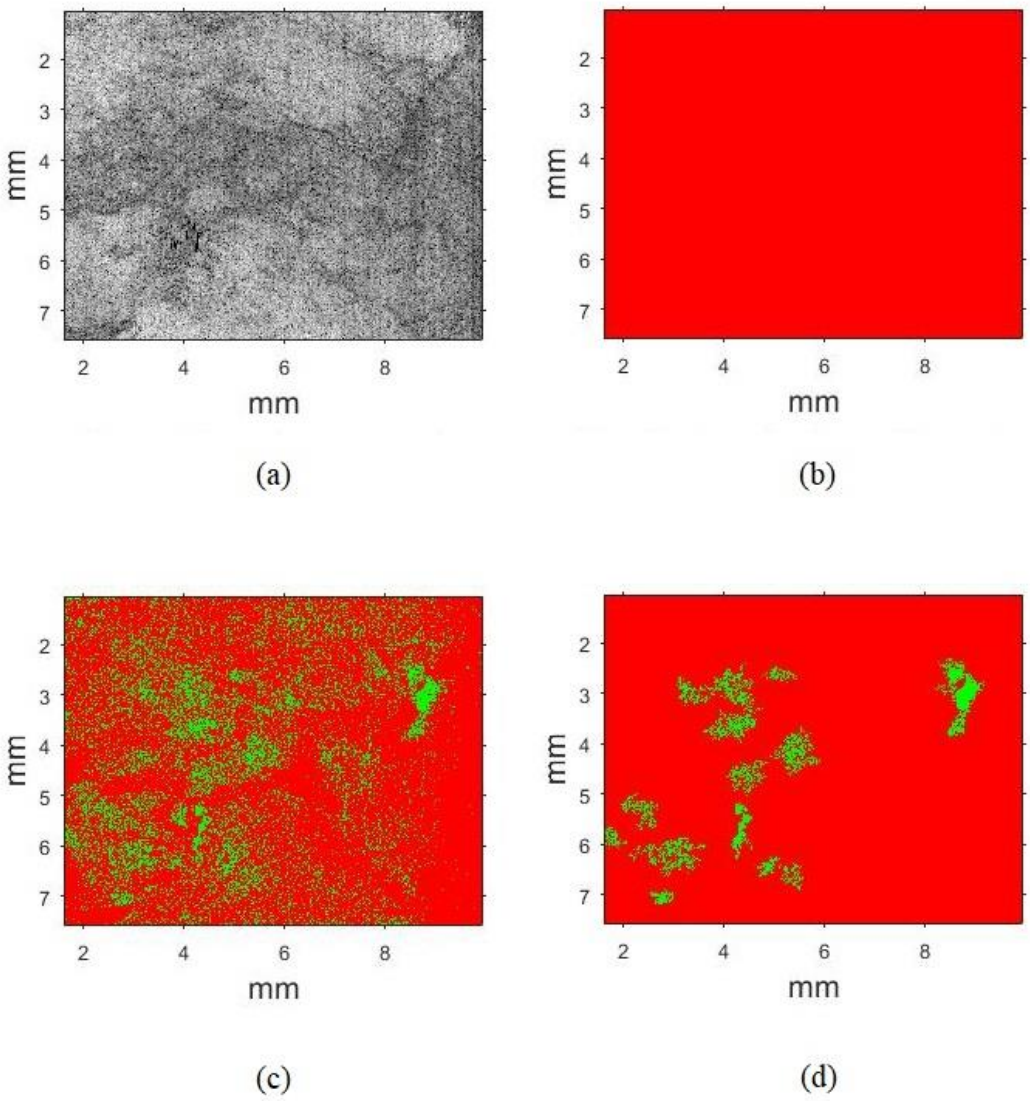

Figure 6.2: Final results of the classification algorithm for the sample of Patient 3 (red = infiltration, green = healthy tissue). For this patient, the sample includes only glioma-infiltrated tissue. **a)** En-face image a 0-depth of the test volume; **b)** Gold standard of the test volume; **c)** color-coded map of the results before optimization; **d)** map of the results after optimization.

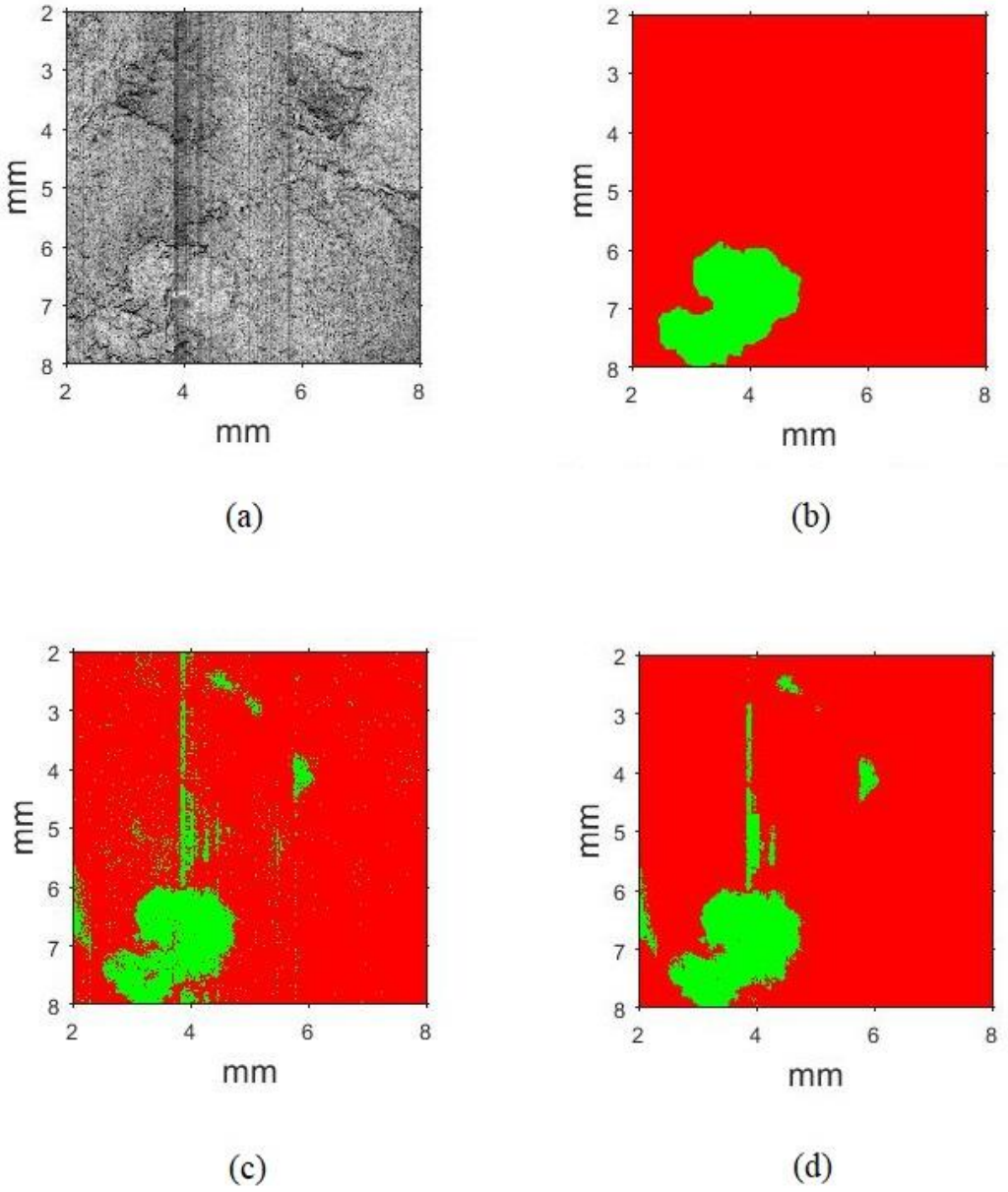

Figure 6.3: Final results of the classification algorithm for the sample of Patient 10 (red = infiltration, green = healthy tissue). This is the only sample that includes both glioma-infiltrated and healthy brain tissue. **a)** En-face image a 0-depth of the test volume; **b)** Gold standard of the test volume; **c)** color-coded map of the results before optimization; **d)** map of the results after optimization.

6.2 3D representation

Classification results, after optimization, are finally displayed in a three-dimensional fashion. The surface of the input sample is represented in 3D with the same codification showed in the previous Section. This is the real output of this algorithm, because it provides to the surgeon a tool for locating in space the network output, by knowing exactly the position of the labeled tissues.

In some cases, infiltrated regions of the sample that are located more in depth, and so out of focus, can be classified as healthy because of their reduced number of useful points along the A-scans. Figures 6.4, 6.5 and 6.6 show the 3D representation of the results for the three patients.

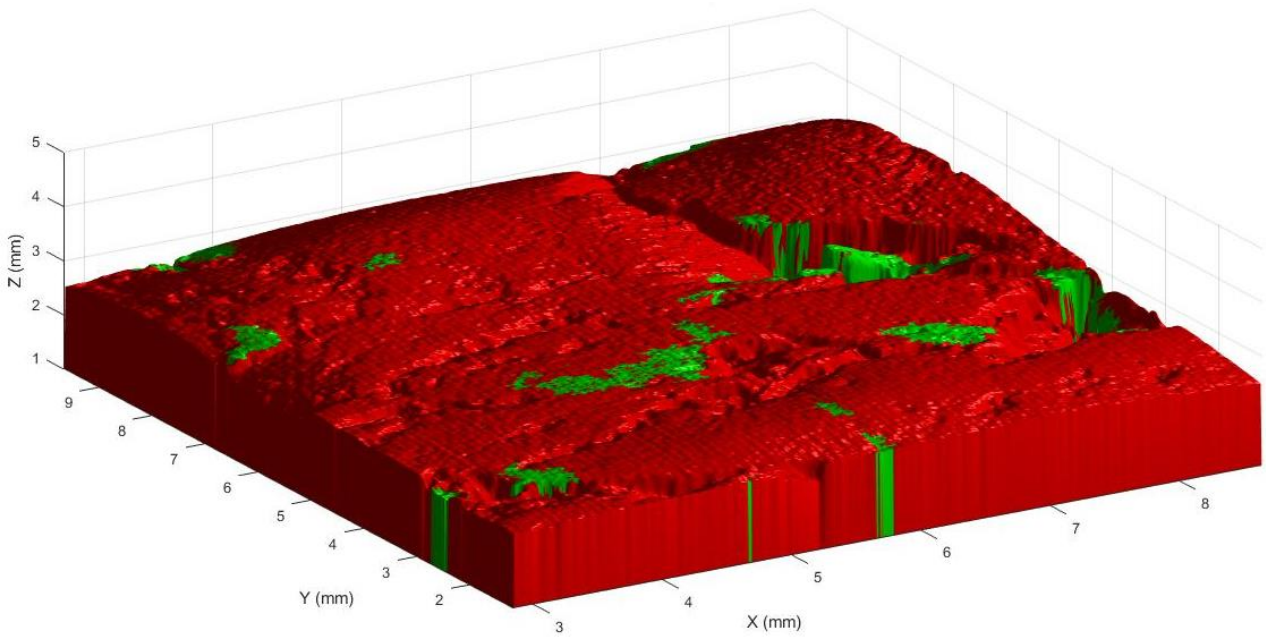

Figure 6.4: 3D representation of the classification output for Patient 2.

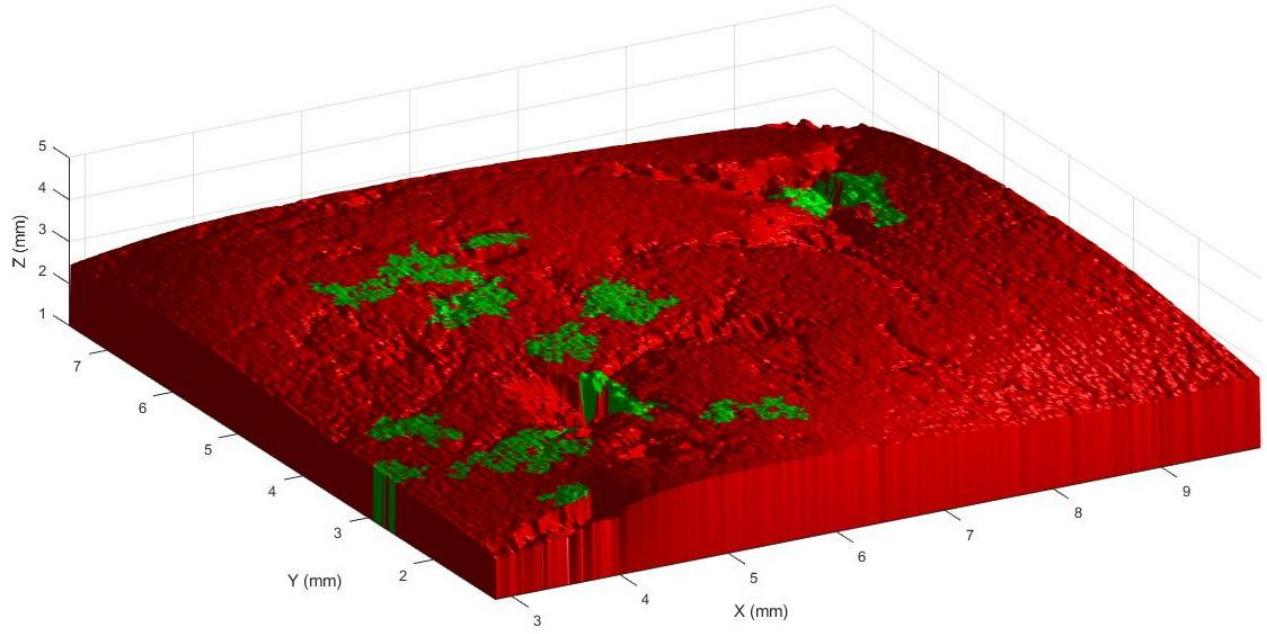

Figure 6.5: 3D representation of the classification output for Patient 3.

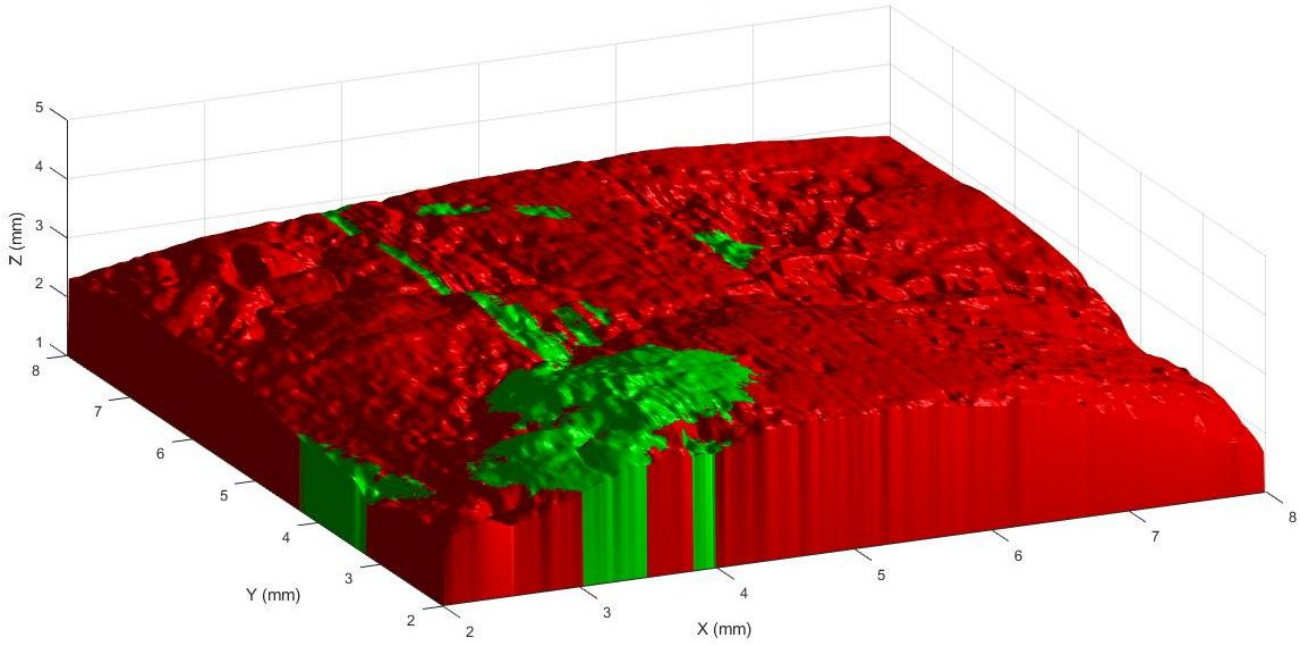

Figure 6.6: 3D representation of the classification output for Patient 10.

6.3 Validation

Validation is carried out to evaluate and quantify the performances of the algorithm. The features used for this purpose, as reported in Paragraph 5.3.2, are:

- Sensitivity
- Specificity
- Positive Predictive Value (PPV)
- Negative Predictive Value (NPV)
- Total Error

The analysis has been made for all the three tissue samples before and after output optimization, to evaluate the improvements introduced by this procedure. Since biopsies taken from patients 2 and 3 do not include healthy brain tissue in their gold standards, the number of 'true negatives' (TN) and 'false positives' (FP) is 0 for both of them, making impossible to calculate Specificity and NPV.

Another consideration to make is about the B-scans corrupted by high-intensity surface reflection artifacts: the averaging method applied to perform the correction, has been executed only on the tomogram of Patient 10, since the other two samples do not show the same grade of corruption, and so, the correction was not necessary.

From the graphs displayed in Figures 6.7 and 6.8, it is clear that the optimization process improves the classification results, especially for the samples of patients 2 and 3. Overall performances (Figure 6.9) have been estimated by summing the three confusion matrices, one for each sample, and computing again the validation features and the total classification error. Once these metrics have been calculated, it is possible to assess the final performances of the algorithm:

Specificity (%)	**Sensitivity (%)**	**PPV (%)**	**NPV (%)**	**Error (%)**
86.48	96.02	99.66	34.23	4.20

Table 6.1: Overall performances of the classification algorithm.

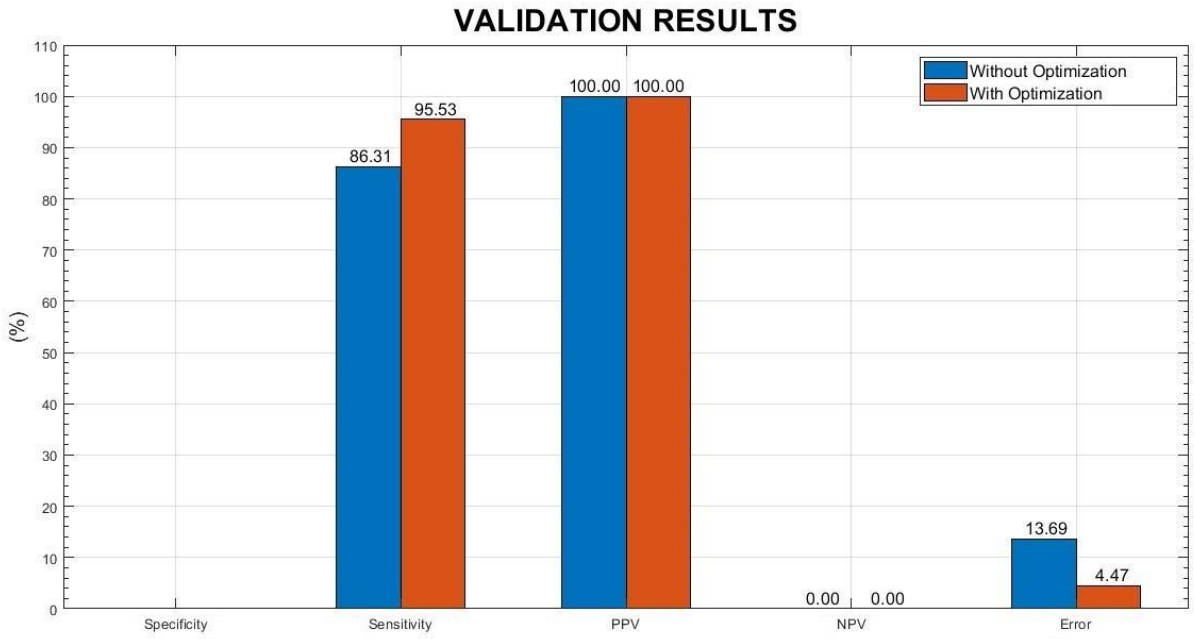

(a)

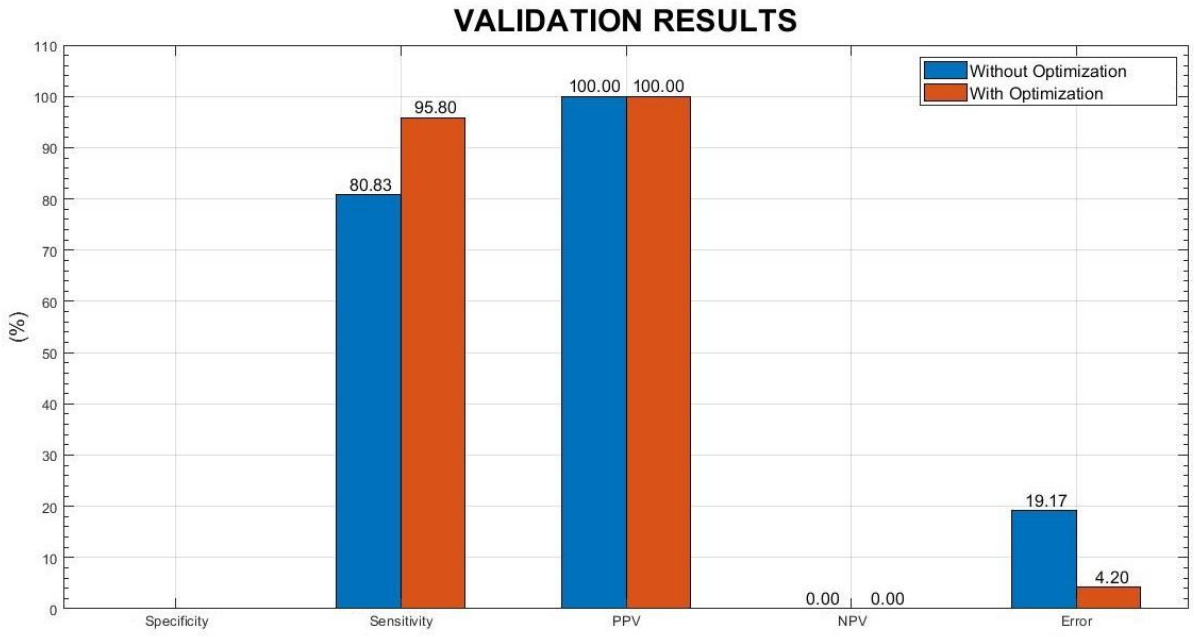

(b)

Figure 6.7: Validation results for the sample of Patient 2 **(a)** and the sample of Patient 3 **(b)**. The four features, along with the total classification error, are computed for two cases: classification without optimization (blue) and classification after optimization (red). For these two samples, the correction of the corrupted B-scans was not necessary.

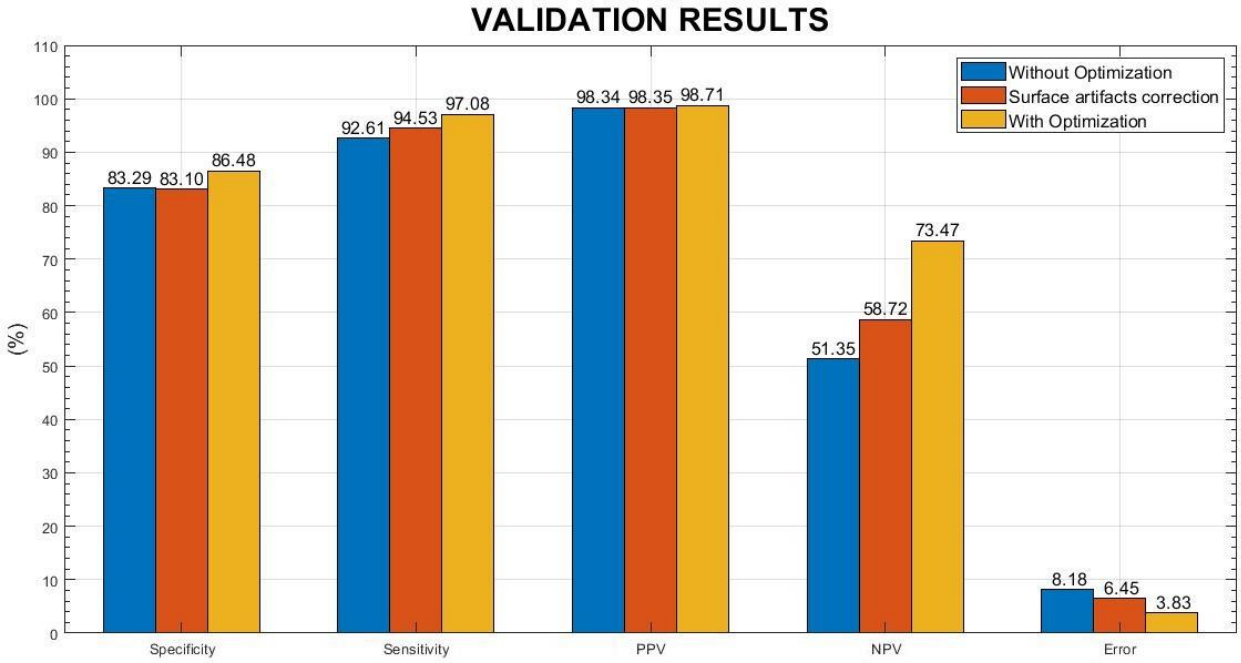

Figure 6.8: Validation results for the sample of Patient 10. The four features, along with the total classification error, are computed for three cases: classification without optimization (blue), classification after surface artifacts corrected with the averaging method (red) and classification after optimization (orange).

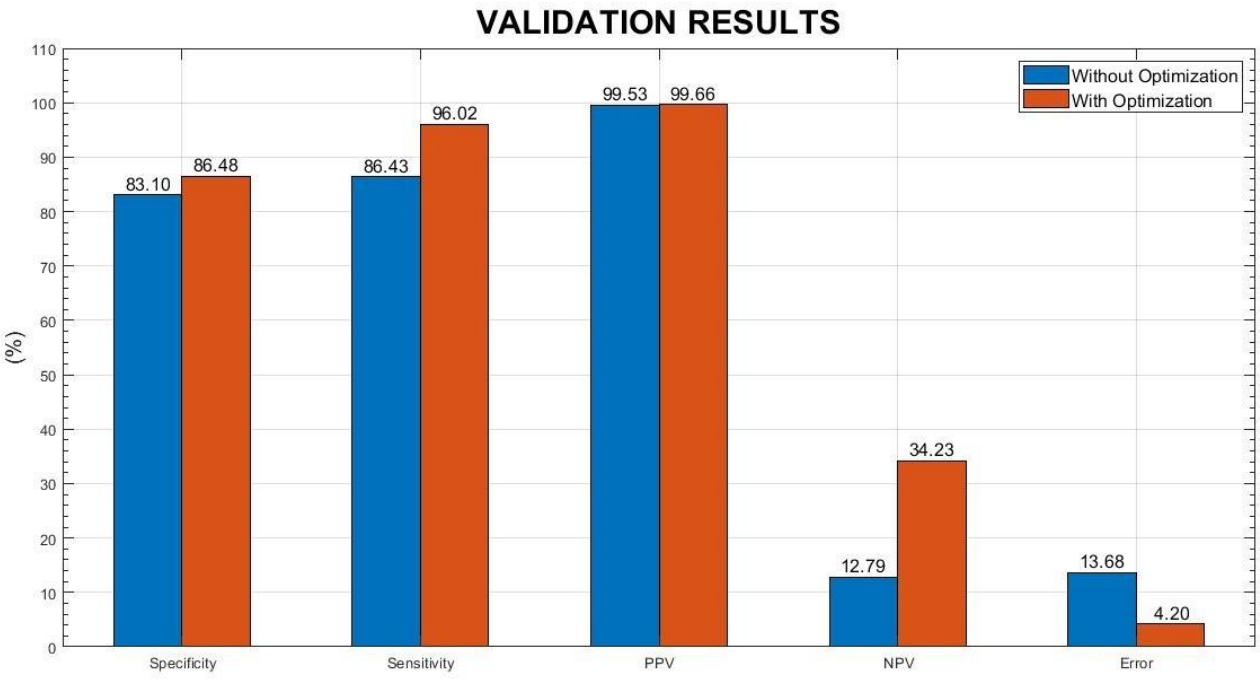

Figure 6.9: Global validation results. The low value of the NPV feature is related to the recognition of small healthy tissue areas where they are not present, but since the real healthy tissue region is highly reduced in size, in respect to the infiltration region, NPV can't reach a high value.

6.3.1 Confront with an alternative classifier

The quality and the robustness of the implemented MLP-Neural Network have been compared with a **second classifier**, created for validation purposes only, that operates on the same test volumes used to evaluate the network. This new algorithm performs the classification task by confronting the envelope of each A-scan with the references found in literature for the two types of tissue. More specifically, for each reference, the classifier calculates the **average point-to-point** distance and the lowest of the two obtained values determines the output label for the A-scan under investigation. Envelopes are obtained by low-pass filtering the trend of the A-line (Figure 6.10), which are then rescaled between the maximum and minimum of the reference envelopes to make a more accurate comparison and normalize the computation. Average distances are then elaborated for the two cases and the output label is set basing on the lower value (Figure 6.11).

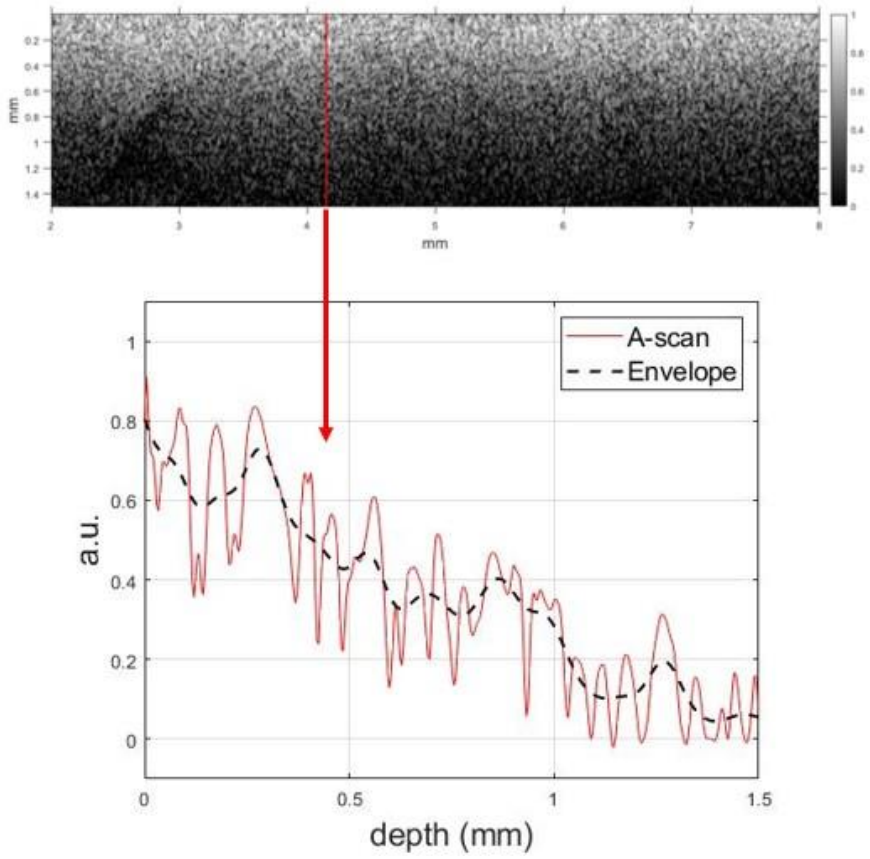

Figure 6.10: A-scan envelope extraction. A low-pass filter of the 30th order is used to obtain the envelope, with cut-off frequency of 0.05 Hz.

The methods used to evaluate the classification outcomes are exactly the same as the ones described in the previous sections of this Chapter, exception made for the 3D representation which, due to the poor quality of the segmentation, has not been carried out. Figure 6.12 shows the overall validation results for this classifier (weak performances in terms of Sensitivity, NPV and classification error) which were then compared to the ones of the Artificial Neural Network (Figure 6.13), demonstrating the higher quality and accuracy of this approach over the new method. As it can be seen, the optimization process worsens the results of the new classifier, since there are large regions of sample that are labeled as 'healthy tissue' but in reality it is all glioma-infiltrated tissue (Figure 6.11).

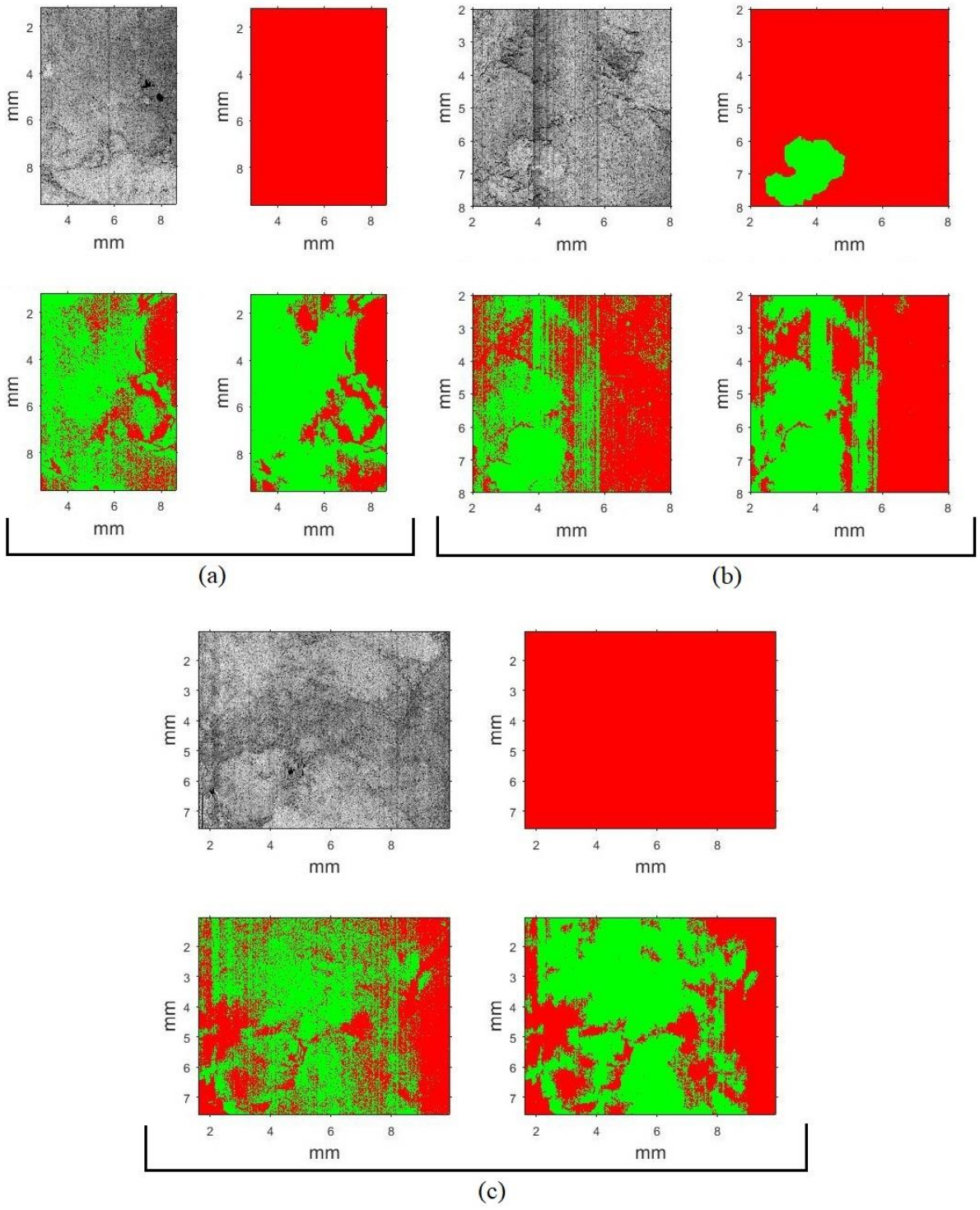

Figure 6.11: En-face map of the results for the alternative classifier. **a)** Results for Patient 2; **b)** results for Patient 10; **c)** results for Patient 3. For each of the three cases: up-left = en-face of test volume; up-right = Gold standard; down-left: classification before optimization; down-right = classification after optimization.

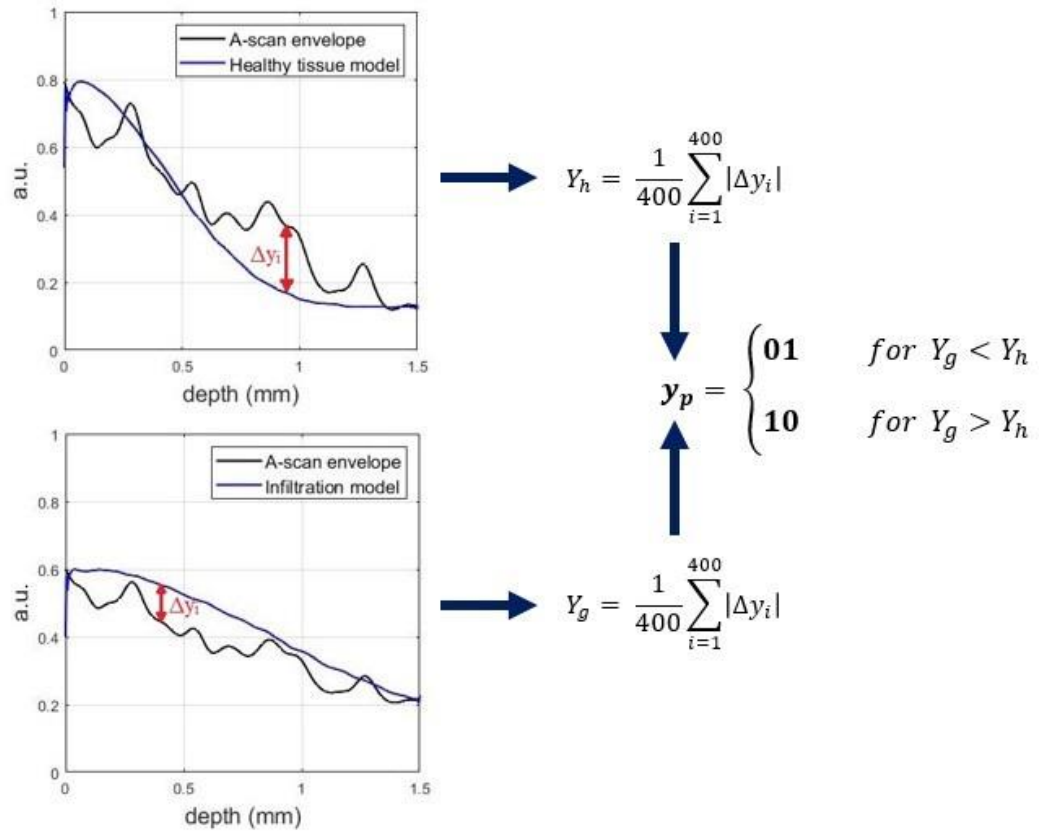

Figure 6.12: Classification method of the alternative algorithm. Y_g and Y_h are the average displacements of glioma-infiltrated and healthy tissue, respectively, while $\boldsymbol{y_p}$ is the predicted class.

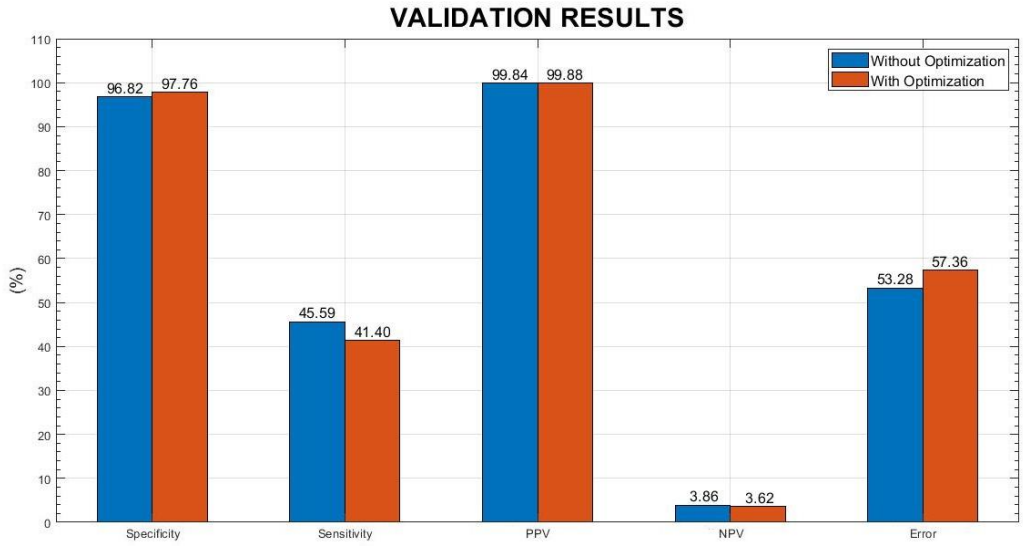

Figure 6.13: Overall validation results of the alternative classifier before and after optimization.

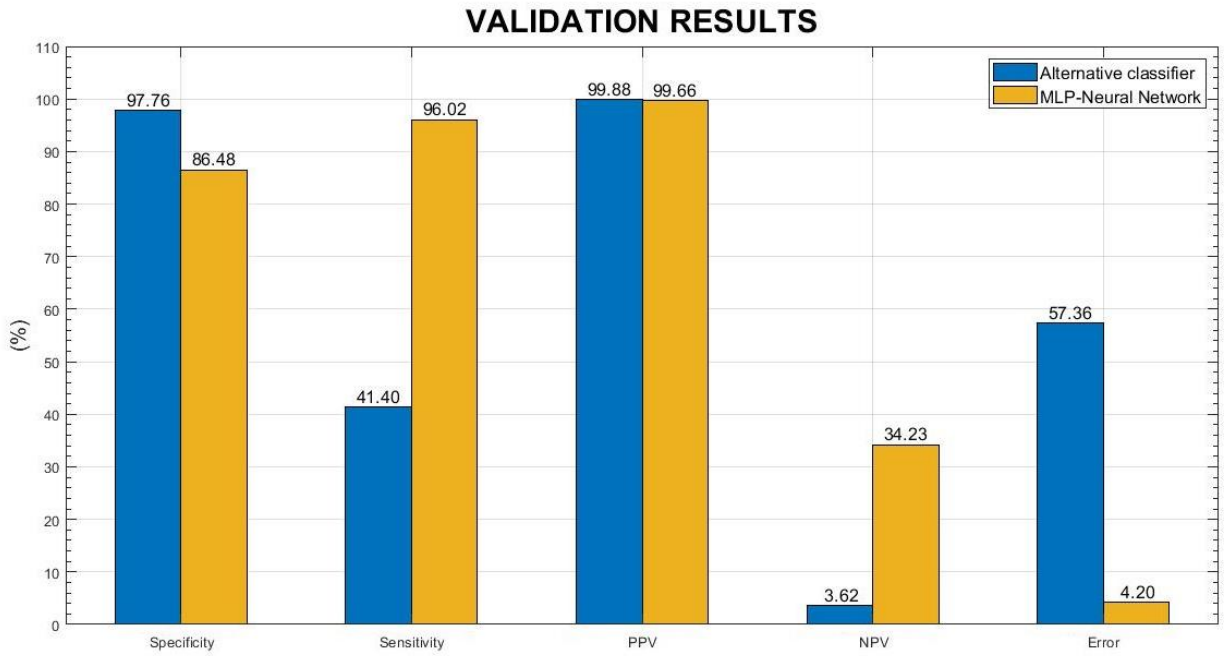

Figure 6.14: Comparison of the performances between the two classifiers.

The alternative algorithm seems to be highly specific in detecting healthy brain tissue, but this is only due to the fact that it recognizes all the healthy tissue, but also classifies as such many other areas that do not belong to this class; this consideration also explains why the Sensitivity is so low. From a general point of view, the new classifier cannot compete with the performances of the developed MLP-Neural Network.

Chapter 7

Conclusions

The Multilayer perceptron Neural Network implemented in this Thesis work exhibits good accuracy in the classification between glioma-infiltrated and healthy brain tissue. Overall performances demonstrate that this algorithm is highly sensitive towards tumor infiltration, despite his specificity is undermined by both surface reflection artifacts and inner defects of the sample under imaging. Further developments are required to overcome these problems and improve the final segmentation.

Silicone phantoms show encouraging results in mimicking the tissues under exam and are suitable to train the network, avoiding the use of real tissue for this specific task. More tests must be carried out to establish the optimal concentrations of Titanium dioxide nanoparticles and Black pigment, but the ones used in this project are indeed a good starting point for the production of simple and replicable tools with homogeneous optical properties.

Summarily, the proposed approach can lead to the development of an intraoperative device which supports the surgeon in distinguishing between the two investigated tissues, helping him in achieving the goal of maximal tumor resection.

Future developments can include:

- Increase of healthy brain tissue samples to enlarge the test dataset and produce more general and reliable validation results.

- The total processing pipeline requires ~30 minutes to be performed, despite network output can be available in maximum a few seconds; the use of a dedicated GPU can lead to real time results.

- Phantoms and brain samples can be imaged with different OCT systems to compare and normalize the performances.

Bibliography

[1] D. N. Louis, A. Perry, G. Reinferberger, A. von Deimling, D. Figarella-Branger, W. K. Cavenee, H. Ohgaki, O. D. Wiestler, P. Kleihues and D. W. Ellison, "The 2016 World Health Organization Classification of Tumors of the Central Nervous System: a summary," *Acta Neuropathol,* pp. 131:803-820, 9 May 2016.

[2] M. Weller, W. Wick, K. Aldape and M. Brada, "Glioma," *Nature,* vol. 1, July 2015.

[3] M. Wank, D. Schilling, T. E. Schmid and B. Meyer, "Human Glioma Migration and Infiltration Properties as a Target for Personalized Radiation Medicine," *Cancers,* no. 10, pp. 456-469, November 2018.

[4] B. Montcel, L. Mahieu-Williame, X. Armoiry, D. Meyronet and J. Guyotat, "Two-peaked 5-ALA-induced PpIX fluorescence emission spectrum distinguishes glioblastomas from low grade gliomas and infiltrative component of glioblastomas," *Biomed. Opt. Express,* vol. 4, no. 4, pp. 548-558, 1 April 2013.

[5] R. M. Juarez-Chambi, C. Kut, K. L. Chaichana, A. Quinones-Hinojosa, X. Li and J. Jo, "Neural networks for in situ detection of glioma infiltration using optical coherence tomography," *SPIE (conference paper),* May 2020.

[6] A. F. Fercher, W. Drexler, C. K. Hitzenberger and T. Lasser, "Optical coherence tomography—principles and applications," *Reports of Progress in Physics,* vol. 66, pp. 239-303, 20 January 2003.

[7] C. E. Flores-Domunguez. e. al, "Low Coherence Optic Source Characterization," *Journal of Physics: Conference Series,* no. 582, 2015.

[8] W. Drexler, M. Liu, A. Kumar, T. Kamali, A. Unterhuber and R. A. Leitgeb, "Optical coherence tomography today: speed, contrast, and multimodality," *Journal of Biomedical Optics,* vol. 19, no. 7, 31 July 2014.

[9] M. Ali and R. Parlapalli, "Signal Processing Overview of Optical Coherence Tomography Systems for Medical Imaging," June 2010. [Online].

[10] O. Sieryi, A. Popov, V. Kalchenko, A. Bykov and I. Meglinski, "Tissue-mimicking phantoms for biomedical applications," *Proceedings of SPIE,* no. 11363, May 2020.

[11] F. Ayers, A. Grant, D. Kuo, D. J. Cuccia and A. J. Durkin, "Fabrication and characterization of silicone-based tissue phantoms with tunable optical properties in the visible and near infrared domain," *Proceedings of SPIE,* vol. 6870, February 2008.

[12] S. A. Prahl, M. J. C. v. Gemert and A. J. Welch, "Determining the optical properties of turbid media by using the adding-doubling method," *Appl. Opt.,* vol. 32, no. 4, pp. 559-568, 1993.

[13] E. A. Genina, A. N. Bashkatov, D. K. Tuchina, P. A. D. Timoshina, N. Navolokin, A. Shirokov, A. Khorovodov, A. Terskov, M. Klimova, A. Mamedova, I. Blokhina, I. Agranovich, E. Zinchenko, O. V. Semyachkina-Glushkovskaya and V. V. Tuchin, "Optical properties of brain tissues at the different stages of glioma development in rats: pilot study," *Biomedical Optics Express,* vol. 10, no. 10, p. 5182–5197, October 2019.

[14] V. M. Kodach, J. Kalkman, D. J. Faber and T. G. v. Leeuwen, "Quantitative comparison of the OCT imaging depth at 1300 nm and 1600 nm," *Biomedical Optics Express,* vol. 1, no. 1, pp. 176-185, August 2010.

[15] J. Fu, G. Quan and H. Gong, "A SIMPLE METHOD FOR PREDICTION OF THE REDUCED SCATTERING COEFFICIENT IN TISSUE-SIMULATING PHANTOMS," *Journal of Innovative Optical Health Sciences,* vol. 3, no. 1, pp. 53-59, 2010.

[16] A. V. Bykov, A. P. Popov, A. V. Priezzhev and R. Myllylä, "Multilayer tissue phantoms with embedded capillary system for OCT and DOCT imaging," *SPIE-OSA,* vol. 8091, 6 June 2011.

[17] R. M. Juarez-Chambi, C. Kut, J. J. Rico-Jimenez, K. L. Chaichana, J. Xi, D. U. Campos-Delgado, F. J. Rodriguez, A. Quinones-Hinojosa, X. Li and J. A. Jo, "AI-Assisted In Situ Detection of Human Glioma Infiltration Using a Novel Computational Method for Optical Coherence Tomography," *Clinical Cancer Research,* vol. 25, no. 21, pp. 6329-6338, November 2019.

[18] I. C. Education, "IBM," 17 August 2020. [Online]. Available: https://www.ibm.com/cloud/learn/neural-networks. [Accessed 30 August 2021].

[19] P. Golik, P. Doetsch and H. Ney, "Cross-Entropy vs. Squared Error Training: a Theoretical and Experimental Comparison," in *14th Annual Conference of the International Speech Communication Association*, 2013.

[20] J. Brownlee, "Gentle Introduction to the Adam Optimization Algorithm for Deep Learning," 3 July 2017. [Online]. Available: https://machinelearningmastery.com/adam-optimization-algorithm-for-deep-learning/. [Accessed 4 April 2021].

[21] S. Doshi, "Various Optimization Algorithms For Training Neural Network," 13 January 2019. [Online]. Available: https://towardsdatascience.com/optimizers-for-training-neural-network-59450d71caf6. [Accessed 4 April 2021].

[22] A. B. I. U. L. N. M. a. N. N. Andrea Shergalis, "Current Challenges and Opportunities in Treating Glioblastoma," *Pharmacological Reviews,* vol. 70, pp. 412-445, July 2018.

[23] S. Kishi, "Impact of swept source optical coherence tomography on ophthalmology," *Taiwan Journal of Ophtalmology,* vol. 6, no. 2, pp. 58-68, June 2016.

[24] J. Jordan, "Setting the learning rate of your neural network," 1 March 2018. [Online]. Available: https://www.jeremyjordan.me/nn-learning-rate/. [Accessed 15 September 2021].

[25] Z. Chen, M. Liu, M. Minneman, L. Ginner, E. Hoover, H. Sattmann, M. Bonesi, W. Drexler and a. Leitgeb., "Phase-stable swept source OCT angiography in human skin using an akinetic source," *Biomedical optics express,* vol. 7, no. 8, pp. 3032-3048, 2016.

[26] J. R. Jayawardana and T. S. Bandaranayake, "Analysis of Optimizing Neural Networks and Artificial Intelligent models for guidance, control and navigation systems," *International Research Journal of Modernization in Engineering, Technology and Science,* vol. 3, no. 3, pp. 743-759, March 2021.